

# Modeling dust mineralogical composition: sensitivity to soil mineralogy atlases and their expected climate impacts

María Gonçalves Ageitos<sup>1,2</sup>, Vincenzo Obiso<sup>3,2</sup>, Ron L. Miller<sup>3,4</sup>, Oriol Jorba<sup>2</sup>, Martina Klose<sup>2,5</sup>, Matt Dawson<sup>2,6</sup>, Yves Balkanski<sup>7</sup>, Jan Perlwitz<sup>3,8</sup>, Sara Basart<sup>2</sup>, Enza Di Tomaso<sup>2</sup>, Jerónimo Escribano<sup>2</sup>, Francesca Macchia<sup>2</sup>, Gilbert Montané<sup>2</sup>, Natalie M. Mahowald<sup>9</sup>, Robert O. Green<sup>10</sup>, David R. Thompson<sup>10</sup>, and Carlos Pérez García-Pando<sup>2,11</sup>

<sup>1</sup>Projects and Construction Engineering Department. Universitat Politècnica de Catalunya, Terrassa, Spain

<sup>2</sup>Barcelona Supercomputing Center, Barcelona, Spain

<sup>3</sup>NASA Goddard Institute for Space Studies, New York, NY, USA

<sup>4</sup>Department of Applied Physics and Applied Mathematics, Columbia University, New York, NY, USA

<sup>5</sup>Department Troposphere Research, Institute of Meteorology and Climate Research (IMK-TRO), Karlsruhe Institute of Technology (KIT), Karlsruhe, Germany

<sup>6</sup>Currently at Atmospheric Chemistry Observations and Modeling Laboratory, National Center for Atmospheric Research, Boulder, Colorado, USA

<sup>7</sup>Laboratoire des Sciences du Climat et de l'Environnement, Gif-sur-Yvette, France

<sup>8</sup>Climate, Aerosol, and Pollution Research, LLC, Bronx, NY, USA

<sup>9</sup>Cornell University, Ithaca, NY, USA

<sup>10</sup>Jet Propulsion Laboratory, California Institute of Technology, Pasadena, CA, USA

<sup>11</sup>ICREA, Catalan Institution for Research and Advanced Studies, Barcelona, Spain

**Correspondence:** María Gonçalves Ageitos (maria.goncalves@upc.edu, maria.goncalves@bsc.es)

## Abstract.

Soil dust aerosols are a key component of the climate system, as they interact with short- and long-wave radiation, alter cloud formation processes, affect atmospheric chemistry and play a role in biogeochemical cycles by providing nutrient inputs such as iron and phosphorus. The influence of dust on these processes depends on its physico-chemical properties, which far from being homogeneous, are shaped by its regionally varying mineral composition. The relative amount of minerals in dust depends on the source region and shows a large geographical variability. However, many state-of-the-art Earth System Models (ESMs), upon which climate analyses and projections rely, still consider dust mineralogy as invariant. The explicit representation of minerals in ESMs is more hindered by our limited knowledge of the global soil composition along with the resulting size-resolved airborne mineralogy than by computational constraints. In this work we introduce an explicit mineralogy representation within the state-of-the-art atmosphere-chemistry model MONARCH. We review and compare two existing soil mineralogy datasets, which remain a source of uncertainty for dust mineralogy ~~modelling~~modeling, and provide an evaluation of multi-annual simulations against available mineralogy observations. Soil mineralogy datasets are based on measurements performed after wet sieving, which breaks the aggregates found in the parent soil. Our model predicts the emitted particle size distribution (PSD) in terms of its constituent minerals based on Brittle Fragmentation Theory (BFT), which reconstructs the emitted mineral aggregates destroyed by wet sieving. Our simulations broadly reproduce the most abundant mineral fractions, independently of the soil composition data used. Feldspars and calcite are highly sensitive to the soil mineralogy map, mainly

due to the different assumptions made in each soil dataset to extrapolate a handful of soil measurements to arid and semi-arid regions worldwide. For the least abundant or more difficult to determine minerals, such as the iron oxides, uncertainties in soil mineralogy yield differences in annual mean aerosol mass fractions of up to  $\sim 100\%$ . Although BFT restores coarse aggregates including phyllosilicates that usually break during soil analysis, we still identify an overestimation of coarse quartz mass fractions (above  $2\text{ }\mu\text{m}$  in diameter). In a dedicated experiment, we estimate the fraction of dust with undetermined composition as given by a soil map, which makes a  $\sim 10\%$  of the emitted dust mass at the global scale, and can be regionally larger. Changes in the underlying soil mineralogy impact our estimates of climate-relevant variables, particularly affecting the regional variability of the single scattering albedo at solar wavelengths, or the total iron deposited over oceans. All in all, this assessment represents a baseline for future model experiments including new mineralogical maps constrained by high quality spaceborne hyperspectral measurements, such as those arising from the NASA EMIT mission.

## 1 Introduction

Airborne dust is one of the most abundant aerosols in the atmosphere and a fundamental component of the Earth system (e.g., Miller et al., 2014). Dust scatters and absorbs short- and long-wave radiation (e.g., Di Biagio et al., 2017, 2019; Obiso et al., in prep., b) (e.g., Di Biagio et al., 2017, 2019), affects cloud-formation processes (e.g., Atkinson et al., 2013; Harrison et al., 2019; Chatziparaschos et al., 2023), atmospheric chemistry and biogeochemical cycles (e.g., Krueger et al., 2004; Myriokefalitakis et al., 2022) (e.g., Krueger et al., 2004; Jickells, 2005; Kanakidou et al., 2018). All these processes are sensitive to dust mineralogy, as dust is present in soils and in the atmosphere as a mixture of different minerals with varying physico-chemical properties, rather than a homogeneously mixed species.

Iron oxides are effective absorbers of short-wave radiation (Sokolik and Toon, 1996, 1999; Moosmuller et al., 2012; Wagner et al., 2012; Sokolik and Toon, 1996, 1999; Moosmuller et al., 2012; Wagner et al., 2012; Di Biagio et al., 2019), while minerals like calcite, quartz or phyllosilicates interact mostly with thermal radiation (Sokolik et al., 1998; Di Biagio et al., 2014, 2017). Dust particles chemically age in the atmosphere, getting coated by acids (such as sulphuric acid, nitric acid or chlorine), or organic species (Goodman et al., 2000). The uptake rates of such compounds on dust aerosols are enhanced by the amount of calcite and other alkaline components present (Krueger et al., 2004; Zakoura et al., 2020). Due to these coatings, originally hydrophobic dust becomes hygroscopic, which favors cloud formation processes (Usher et al., 2002). In addition, k-feldspars and quartz (Zimmermann et al., 2008; Atkinson et al., 2013; Harrison et al., 2019) have been revealed as efficient ice nuclei, compared to other minerals present in dust, and their presence can enhance the generation of mixed-phase clouds (Chatziparaschos et al., 2023) (e.g., Chatziparaschos et al., 2023). Finally, iron and/or phosphorous species in mineral dust act as micro-nutrients for ocean and terrestrial ecosystems, influencing the global carbon, phosphorus and nitrogen biogeochemical cycles (Mahowald et al., 2008; Yu et al., 2015; Ito and Shi, 2016; Wang et al., 2017) (Mahowald et al., 2008; Yu et al., 2015; Ito and Shi, 2016). In particular, atmospheric soluble iron deposition constitutes a controlling factor of primary productivity in certain open ocean regions (Jickells, 2005). Although the solubility of freshly emitted iron from dust sources is relatively low, it gets enhanced during transport owing to atmospheric processing mechanisms. Both the amount of iron emitted from dust sources and its suscepti-

50 bility to become soluble in the atmosphere depend on the dust composition (Journet et al., 2008; Shi et al., 2011, 2012; Myriokefalitakis et al., 2018, 2022).

However, many state-of-the-art Earth System Models (ESMs) do not account for this information and still consider dust as a homogeneous species, mainly due to the existing uncertainties in the size-resolved composition of parent soils and the resulting size distribution of minerals in airborne dust, as well as the scarcity of observations to constrain them, but also because of computational constraints.

Atmospheric dust occurs due to soil particles lifting from the Earth surface, primarily from arid and semi-arid regions. The direct action of wind and turbulent forces, as well as the impact of saltating grains, act on the erodible surface layer of the soil to produce emission of particles mostly in the clay (up to 2  $\mu\text{m}$  in diameter) and silt size ranges (from 2 to 63  $\mu\text{m}$  in diameter). Therefore, the size-dependent composition of the parent soil determines the mineralogy of the emitted dust. Observations show a distinctive composition of airborne dust originating from different source regions. Mineralogy is often inferred from elemental composition analyses or determined through semi-quantitative methods (Kandler et al., 2007, 2009; Scheuvens et al., 2013; Panta et al., 2022). Airborne dust samples are usually scarce, and many times these are complemented with artificially resuspended soil samples in the laboratory, through experimental setups designed to mimic dust emission, or with dust deposition and sediment samples (Kandler et al., 2007, 2009; Lawrence and Neff, 2009; Scheuvens et al., 2013).

Regional variations in dust mineralogy are commonly associated with changes in soil geology or weathering processes (Claquin et al., 1999; Scheuvens et al., 2013). Chemical weathering is enhanced in warm wet climates compared to dry cold climates. Some minerals, e.g., quartz, are insensitive to chemical weathering, while others are more susceptible to change and lead to the formation of secondary minerals (e.g., the hydrolysis of feldspars forms kaolinite, or the oxidation of ferromagnesian silicates produces secondary iron oxides). These factors explain, for instance, why dust from the Sahel region, characterized by intense weathering, is richer in kaolinite than that from the Saharan sources (Chester et al., 1972; Caquineau et al., 2002), and it has a high iron oxides content (Formenti et al., 2008, 2014). Chlorite is usually more abundant in dust from high latitudes (Griffin et al., 1968; Chester et al., 1972; Kandler et al., 2020). A latitudinal gradient of calcite, quartz and illite is also found in dusts originated in North African sources, with decreasing mass fractions towards the equator (Chester et al., 1972; Chiapello et al., 1997; Caquineau et al., 1998, 2002; Lafon et al., 2006; Formenti et al., 2008). Particularly, the abundance of carbonates in the North and North-West Saharan dusts is related to the soil geology from these areas, which are dominated by limestones and carbonate-rich soils, i.e., calcisols (Scheuvens et al., 2013; Formenti et al., 2011). Central Asian sources are rich in quartz (Gomes and Gillette, 1993), illite or chlorite (Gomes and Gillette, 1993; Lafon et al., 2006; Kandler et al., 2020). There are also evidences of dust mineralogical composition changes with transport. Typically, coarse-grained minerals, such as feldspars or quartz, constitute a higher fraction of transported mass close to sources compared to samples collected in remote regions, where smaller phyllosilicates are more abundant (Lawrence and Neff, 2009).

Despite these evidences, our knowledge of soil mineralogy at the global scale relies exclusively on a scarce set of soil descriptions. These measurements are particularly rare in the arid and semi-arid regions prone to dust emission, and usually provide only a crude representation of the size distribution. Exploiting this information, previous works (Claquin et al., 1999;

Nickovic et al., 2012; Journet et al., 2014; Ito and Wagai, 2017) have developed soil mineralogy maps, oriented to atmospheric and climate ~~modelling~~modeling, which provide the mineral mass fractions present in the clay and silt size ranges.

The earliest Soil Mineralogy Atlas (SMA) used for atmospheric studies, by Claquin et al. (1999), reports eight different minerals relevant for their climate effects, namely: illite, smectite, kaolinite, calcite, quartz, feldspars, gypsum and hematite. The latter is commonly taken as a proxy for iron oxides (mainly hematite and goethite), and although originally apportioned exclusively to the silt size, further extensions of the soil map (Nickovic et al., 2012) consider iron oxides to be also present in the finer clay sizes. This updated size distribution has been proved to be more realistic through modelling studies (Scanza et al., 2015; Perlwitz et al., 2015a, b). A more recent map by Journet et al. (2014) reports four additional minerals, including chlorite, vermiculite, and mica, and distinguishing between hematite in the clay and goethite in the clay and silt sizes of the soil. Ito and Wagai (2017) introduce novel approaches to quantify the existing uncertainties in our knowledge of top- and sub-soil composition of clay-sized minerals. Unfortunately, their study neglects the silt-sized grains, which prevents modellers from having consistent information throughout the size ranges of airborne dust.

These maps are built upon soil descriptions usually obtained through experimental techniques that break the aggregates originally present in the soil (i.e., wet sieving). As a result, phyllosilicates, which are usually emitted as aggregates, are overemphasized in the finer soil fractions compared to what is observed in airborne dust. Soil analyses may also alter the size distribution of carbonates, such as calcite. Some ~~modelling~~modeling studies directly attribute the soil minerals' size distribution to the airborne dust (e.g. Atkinson et al., 2013; Ito and Xu, 2014). However, novel approaches have been introduced by Perlwitz et al. (2015a, b); Scanza et al. (2015) and Pérez García-Pando et al. (2016), relying on the Brittle Fragmentation Theory (BFT) (Kok, 2011), which allow to represent the emitted mineral size distribution more realistically.

A range of previous ~~modelling~~modeling studies have focused on constraining the influence of mineralogy on the dust Direct Radiative Effect (DRE). Non-negligible impacts on dust absorption have been identified, either using the raw mineral variations in the soil (~~Claquin et al., 1999~~)(e.g., Claquin et al., 1999), directly translating ~~those~~them into airborne mass fractions (~~Journet et al., 2014~~)(e.g., Journet et al., 2014; Ito et al., 2018), or redistributing the minerals into the emitted sizes through BFT (~~Scanza et al., 2015~~)(e.g., Scanza et al., 2015; Obiso et al., 2023). Particularly, our poor knowledge of the abundance of iron oxides and their speciation has been identified as a key factor contributing to the uncertainty in ~~modelled~~modeled dust DRE, in one of the few analysis to date which considers not only the mean mineralogy, but also the ranges of variability provided with the soil maps (Li et al., 2021). Despite these uncertainties, ~~there are evidences that accounting for the soil's varying composition improves~~ the spatio-temporal variability in ~~modelled dust absorption when considering the soils' varying composition gets closer to that observed, independently of the soil information used~~ (Obiso et al., in prep., a) modeled dust absorption as compared to observations (Obiso et al., 2023).

Some models already incorporate explicitly the number concentration of K-feldspar and quartz in the atmosphere (Atkinson et al., 2013; Vergara-Temprado et al., 2017; Chatziparaschos et al., 2023) ~~, proving that these estimates have a positive impact on the modelled to derive the concentration of~~ ice nucleating particles ~~as compared to observations~~ (INPs). ~~Their evaluation against observations suggests improvements in the geographical distribution of the INPs~~ (Atkinson et al., 2013), ~~as well as their relevance at the global scale~~ (Vergara-Temprado et al., 2017; Chatziparaschos et al., 2023). Dust mineralogy has



been also been considered in models to derive the total iron content and its potential solubility through atmospheric processing

(Johnson and Meskhidze, 2013; Ito and Xu, 2014; Myriokefalitakis et al., 2018; Hamilton et al., 2019; Myriokefalitakis et al., 2022; ?) (e.g. Johnson and Meskhidze, 2013; Ito and Xu, 2014; Wang et al., 2015; Ito and Shi, 2016; Ito et al., 2018; Scanza et al., 2018; Myriokefalitakis et al., 2022), with the aim of assessing its effect on soluble iron deposition over the ocean, and hence on primary productivity and biogeochemical cycles.

From these efforts, only a few (Perlwitz et al., 2015a, b; Scanza et al., 2015; Pérez García-Pando et al., 2016; Hamilton et al., 2019; Li et al., 2021; Myriokefalitakis et al., 2022) consider the difference between the size distribution of minerals reported in the soil maps and that of the aerosol, and even fewer (Li et al., 2021) make use of different soil maps in a common modelling framework model.

To our knowledge, a systematic evaluation of the impact of the choice of a specific soil mineralogy map in the modelled modeled airborne mineralogy has not been conducted, although such a choice has a potentially relevant effect on the modelled modeled atmospheric composition and climate. To that end, we extend the atmospheric dust cycle of the Multiscale Online Nonhydrostatic Atmosphere Chemistry (MONARCH) model (Klose et al., 2021, and references therein) to allow for an explicit representation of the different minerals present in dust aerosols. We review and assess the SMAs from Claquin et al. (1999), with the updates by Nickovic et al. (2012), and Journet et al. (2014), and we conduct three different global multi-annual experiments in which we exclusively vary the soil composition information. We compare our model results to available observations of dust mineralogy to provide an overall assessment of the model capabilities and the weaknesses and strengths of the soil mineralogy choice. Finally, we derive proxies that allow us to assess the impact of the modelled modeled mineralogy on key climate aspects, such as the dust DRE and the atmospheric soluble iron deposition. Our study represents the baseline upon which simulations including soil mineralogy maps built with new high-quality spaceborne hyperspectral information (Green et al., 2020) will be compared in the near future.

## 2 Modelling Modeling dust mineralogy in MONARCH

### 2.1 The Atmospheric Chemistry Model

MONARCH is a fully coupled atmosphere chemistry model developed at the Earth Sciences Department of the Barcelona Supercomputing Center (BSC). The model's atmospheric dynamics rely on the Non-hydrostatic Multiscale Model on the B-grid (NMMB) (Janjic and Gall, 2012), which can be applied from regional to global spatial scales. MONARCH has also inherited from NMMB the ability to use different representations for relevant physics processes (e.g., the land-surface model, or the cloud microphysics representation).

MONARCH includes an in-line gas-phase chemistry module (Jorba et al., 2012; Badia and Jorba, 2015; Badia et al., 2017) and advanced representation of natural and anthropogenic aerosols, namely dust (Pérez et al., 2011; Haustein et al., 2012; Klose et al., 2021), sea salt (Spada et al., 2013), organic mass (primary and secondary), black carbon (Spada, 2015), sulphate, ammonia and nitrate. The dynamic aerosols can interact with short- and long-wave radiation (Pérez et al., 2011). Ongoing developments include the representation of heterogeneous chemistry considering dust mineralogy (Soussé Villa et al., 2021),

and brown carbon and its effects on the atmospheric radiative balance (Navarro-Barboza et al., 2021). At the moment, the aerosol-cloud interactions are not explicitly solved and the cloud activation schemes rely on aerosol climatologies. One of the guiding principles of the model design is flexibility, in a way that allows the user to select the aerosol species to be simulated, the activation or not of the gas-phase chemistry, the coupling of the dynamically represented aerosols with radiation, etc. Also, work is being done to allow the chemistry to be solved using runtime configuration approaches (Dawson et al., 2021) and exploiting GPUs heterogeneous architectures (Guzmán-Ruiz et al., 2020).

MONARCH is a member of the multi-model ensemble of the Copernicus Atmosphere Monitoring Service (CAMS) of the European Commission providing operational air quality forecasts, analyses and reanalyses of the main atmospheric pollutants among reactive gases and aerosols for an extended European domain (Colette et al., in prep.). The MONARCH assimilation system (MONARCH-DA) is based on a Local Ensemble Transform Kalman Filter (LETKF) scheme (Hunt et al., 2007; Miyoshi and Yamane, 2007; Schutgens et al., 2010; Di Tomaso et al., 2017; Escribano et al., 2022) coupled to the model through I/O routines, and which requires the model to be run in an ensemble mode. These complex simulations are handled through the Autosubmit workflow manager (Manubens-Gil et al., 2016; Uruchi et al., 2021), which allows also to process the necessary input files, and to post-process and archive the model outputs in an easy way.

In this work, we apply MONARCH's standard configuration for the physics schemes and parameterizations. This setup counts on the Rapid Radiative Transfer Model, RRTMG (Iacono et al., 2001, 2008) to solve short- and long-wave radiation. The Betts-Miller-Janjic scheme (Betts, 1986; Betts and Miller, 1986) parameterizes convection, while grid-scale precipitation is defined through Ferrier microphysics (Ferrier et al., 2002). Turbulence and the planetary boundary layer rely on the Mellor-Yamada-Janjic scheme (Janjic, 2002; Mellor and Yamada, 1982), and the land surface fluxes, on the Noah model (Ek et al., 2003). All the experiments are configured to represent only the atmospheric dynamics and the speciated dust cycle, disabling the gas-phase chemistry and the other dynamic aerosols. The dust interaction with radiation, along with that of other aerosols, is solved by using prescribed aerosol climatologies. [This configuration allows us to reproduce the main features of the minerals life cycle, while it optimizes the computational time needed to conduct the experiments.](#)

## 2.2 Representation of the dust cycle

The MONARCH dust cycle has been extensively evaluated at regional and global scales (Pérez et al., 2011; Haustein et al., 2012; Klose et al., 2021). The model is the reference forecast system of the Barcelona Dust Forecast Center (<https://dust.aemet.es/>), and the Regional Center for Northern Africa, the Middle East and Europe (NAMEE) of the Sand and Dust Storms Warning Advisory and Assessment System (SDS-WAS) of the World Meteorological Organization (WMO). Moreover, MONARCH has the capability to improve dust estimates through data assimilation techniques, both using column integrated (Di Tomaso et al., 2017; Di Tomaso et al., 2022) and vertically resolved (Escribano et al., 2022) satellite dust retrievals, and it has been recently used to derive a dust regional reanalysis for the NAMEE domain (Di Tomaso et al., 2022) with unprecedented high resolution.

MONARCH represents dust generation and uplift by surface winds and turbulence through a set of different schemes. Then dust aerosols are transported through horizontal and vertical advection, horizontal diffusion and vertical transport by turbulence and convection, and removed from the atmosphere by dry deposition and gravitational settling, and in-cloud and below-cloud

scavenging. The dust size distribution follows a sectional approach and considers eight transport bins ranging up to 20  $\mu\text{m}$  in diameter, with the four finest bins covering the clay size range, and the others falling in the silt size range, in particular: 0.2–0.36, 0.36–0.6, 0.6–1.2, 1.2–2.0, 2.0–3.6, 3.6–6.0, 6.0–12.0, and 12.0–20.0  $\mu\text{m}$  (Pérez et al., 2011; Klose et al., 2021) are the size boundaries for each bin.

190 Dust emission can be defined via a variety of schemes (Klose et al., 2021), ranging from more physics-based to more heuristic approaches (Marticorena and Bergametti, 1995; Ginoux et al., 2001; Shao, 2001, 2004; Shao et al., 2011; Kok et al., 2014). The schemes either produce Particle Size Distributions (PSD) at emission dependent on the atmospheric forces (Shao, 2001), or fix the emitted PSD following either D’Almeida (1987) or Kok (2011).

In this work, we select one of the configurations defined and assessed in Klose et al. (2021) (G01-UST), in which dust  
195 emission relies on a topography-based source function (Ginoux et al., 2001) that scales the flux from potentially available sources and depends on the friction velocity. Dust emission is possible from areas identified through maps of frequency of occurrence of dust optical depth above 0.2 created from Moderate Resolution Imaging Spectroradiometer (MODIS) Deep Blue retrievals (Ginoux et al., 2012; Hsu et al., 2004). The effect of surface roughness is parameterized based on Raupach et al. (1993) using vegetation cover information derived from Landsat and MODIS surface reflectance monthly data (Guerschman  
200 et al., 2015).

### 2.3 Dust mineralogy

A key element to independently trace different minerals is to estimate the size-resolved mineralogy at emission. To do so, we need to (1) define the soil mineralogy at the model grid horizontal resolution ([Section-section 2.3.1](#)), and (2) to project the soil mineralogy onto the transport bin sizes ([Section-section 2.3.2](#)). Then, the emitted mineral mass fractions in each of the  
205 size bins is multiplied by the [modelled-modeled](#) bulk dust flux, and each mineral is independently traced and subjected to the main transport and removal processes. The [representation of the minerals’ size distribution in MONARCH follows that of the compositionally homogeneous dust, i.e., each mineral will be represented by 8 tracers with diameters ranging from 0.2 to 20  \$\mu\text{m}\$](#) . The current implementation allows the user to customize the subset of minerals to be simulated, with the aim of making the model computationally lighter for specific applications.

210 We define mineral-dependent mass densities according to literature data (Table 1). All minerals are considered to be externally mixed, except for iron oxides. A large part of the emitted flux of iron oxides is considered to be internally mixed with other minerals, e.g., in the form of accretions in phyllosilicates, in line with observational evidences and previous [modelling modeling](#) studies (Kandler et al., 2009; Perlwitz et al., 2015a). In MONARCH, we define two different types of tracers for the iron oxides. One set of tracers carries the mass of the iron oxides that constitute accretions in other minerals, which make  
215 up the largest fraction, and are allowed to be up to 5 % of the mass of the other minerals at emission (Perlwitz et al., 2015a). Given that their total emitted mass is low compared to the sum of all minerals, we assume that these accretions do not change the mass density of the host particles and we assign them the density of the most abundant phyllosilicate, i.e., illite. Another set of tracers is used to transport the remaining fraction of iron oxides, which is considered to be externally mixed. Their mass

density depends on the speciation given by the soil map used, either as iron oxides (average between hematite and goethite),  
220 pure hematite or pure goethite.

Mass density impacts the mineral settling velocity, which is particularly relevant for the removal of coarse particles, as well as parameters influencing the wet deposition, which constitutes an effective removal process for finer particles. Below-cloud particle scavenging in MONARCH is defined according to Slinn (1984), and the capture efficiencies for snow and rain droplets change with the mass density, the volume and effective particle radius (see Pérez et al., 2011, for details). At present, minerals  
225 have the same treatment in in-cloud scavenging, i.e., they are assumed to share the same solubility, and they do not chemically interact with other gas-phase or aerosol species in the model. The change in densities with respect to homogeneous dust (set to 2500 kg m<sup>-3</sup> for the 4 finest bins, and to 2650 kg m<sup>-3</sup> for the 4 coarsest bins), together with the preferential size distribution of the minerals (e.g. finer phyllosilicate grains, coarser calcite, quartz and feldspars)~~result,~~ results in differences in the global distribution of minerals with respect to homogeneous dust (see ~~Section~~ section 5.3).

### 230 2.3.1 Soil mineralogy at the model resolution

MONARCH can derive the soil composition of dust sources from the soil map of Claquin et al. (1999), with the modifications by Nickovic et al. (2012), C1999-SMA, or from a revised version of the map from Journet et al. (2014), J2014-SMA. C1999-SMA and J2014-SMA were originally designed with a focus on dust mineralogy ~~modelling~~ modeling, and, as aforementioned, they identify 8 and 12 relevant minerals for dust-climate interactions in the clay and silt fraction of the soil, respectively (see  
235 Appendix A, for details).

Both maps rely on the same basic principle: they hypothesize that mineralogy is inherently linked to the soils physico-chemical properties and texture, which are commonly used in soil classification systems (e.g. those reported by the Food and Agricultural Organization, FAO, of the United Nations). C1999-SMA considers 28 arid and semi-arid soil types identified by the FAO (FAO-UNESCO, 1974), and mapped in the FAO Digital Soil Map of the World (DSMW) (FAO-UNESCO,  
240 1995) with a horizontal resolution of 0.083° (~ 10 km at mid-latitudes). J2014-SMA relies on the FAO74 (FAO-UNESCO, 1974) and FAO90 (FAO-UNESCO, 1997) soil classification, mapped in the Harmonized World Soil Database (HWSD) version 1.1 (FAO/IIASA/ISRIC/ISSCAS/JRC, 2009) with a spatial resolution of 0.0083° (~ 1 km at mid-latitudes). Combining both FAO74 and FAO90 there is a total of 211 different soil units with potential mineralogical content according to J2014-SMA.

Both in C1999-SMA and J2014-SMA, a mean mineralogy is assigned to each soil type or unit by compiling available  
245 descriptions from the literature, and it is subsequently extrapolated geographically to any location that shares the same soil classification, hence providing a spatially resolved map of soil mineral fractions. Despite the extensive data collection, the scarcity of soil composition measurements, their heterogeneity and their uneven geographical distribution challenge the generation of globally representative SMAs. In particular, the available observations at the time allowed Claquin et al. (1999) to describe the mineralogy of 80 % of the soil types they identify as arid or semi-arid. Journet et al. (2014) have observational  
250 information about some of the mineral abundances in 55 % of the 211 FAO74 and FAO90 soil units, and include regions that were not represented in C1999-SMA. However, the compiled observations do not provide information on calcite or iron oxides for many soil units in the clay size fraction, and, in general, there is a misrepresentation of mineralogy of the silt size class.

**Table 1.** Mass densities ( $\text{kgm}^{-3}$ ) and iron content (w%) defined for the minerals included in MONARCH.

Mineral	Density ( $\text{kgm}^{-3}$ )	Iron content (w%)
quartz <sup>(1)</sup>	2670	
calcite <sup>(1)</sup>	2710	
feldspars <sup>(1)</sup>	2680	0.34
gypsum <sup>(1)</sup>	2308	
illite <sup>(1,*)</sup>	2570	4.3
kaolinite <sup>(1)</sup>	2630	0.23
smectite <sup>(1,*)</sup>	2570	2.6
vermiculite <sup>(2)</sup>	2300	6.7
chlorite <sup>(2)</sup>	2420	12.5
mica <sup>(2)</sup>	2810	
iron oxides <sup>(1,**)</sup>	4770	
hematite <sup>(2)</sup>	5210	57.5
goethite <sup>(2)</sup>	4180	62.9

Density values from <https://www.mindat.org/>, <https://www.engineeringtoolbox.com> and <http://www.webmineral.com> as compiled by <sup>(1)</sup> Perlwitz et al. (2015a); and <sup>(2)</sup> Menut et al. (2020); <sup>(\*)</sup> average between illite and smectite; <sup>(\*\*)</sup> average for iron oxides including goethite and hematite. Iron content for phyllosilicate minerals is taken from Journet et al. (2014), and for iron oxides from Journet et al. (2008).

As a result, both maps add empirical relations (e.g., between soil texture and the size distribution of calcite, or the quartz-to-feldspars ratio) and perform additional hypotheses (e.g., associating the soil color to the iron oxides content) to further extend the mineralogical information. In Journet et al. (2014), the distinction in hematite and goethite is sometimes obtained through the application of a fixed ratio based on empirical evidences (Kandler et al., 2009). Furthermore, extensions through averaging of mineral fractions for all the silt-size records, or for major soil groups, are proposed for mica and chlorite, and quartz and feldspars, respectively, to complete the global map (see CASE2 in Journet et al., 2014).

C1999-SMA and J2014-SMA treat differently the components of the soil descriptions that do not correspond to their target minerals, listed in Table 1. While Claquin et al. (1999) report the mineral fractions normalized to sum 100 %, i.e., assume that soil mineralogy fundamentally consists only of the eight identified minerals, Journet et al. (2014) provide the mean mineralogy

as derived from the soil records, with total mass fractions of known minerals ranging from 42.4 % to 102.8 % (without considering inferred calcite fractions, and other extensions). That is, J2014-SMA allows the possibility of emitted minerals that are unidentified and not included in our Table 1. MONARCH can currently use C1999-SMA normalized, and two variations  
265 for J2014-SMA: normalized and not-normalized, which are both based on the extended mineralogy data referred to as CASE2 by Journet et al. (2014). Appendix A describes these datasets (section A1) and summarizes the revision we made (section A2).

One recognized weakness of the methodology to construct the SMAs arises from the main assumption: the link between the defining parameters of a soil class and a mineralogy, which is questionable for some soil classes where the variability in composition among samples is much larger than that of the mean composition. Please, note that, here, we work exclusively  
270 with the information on the mean mineralogy, and we do not consider the uncertainties provided in the original works (i.e., standard deviations of the mineral abundances for each soil type and number of soil descriptions used to derive the values). These uncertainties have been explored for the particular case of iron oxides in previous works (Li et al., 2021), and we plan to consider them in the future to further assess the sensitivity of our ~~modelled~~modeled minerals towards the soil composition.

Although at the regional scale, atmospheric models can reach resolutions as high as that of the SMAs presented here ( $0.0083^\circ$   
275 for J2014-SMA, and  $0.083^\circ$  for C1999-SMA), this is rarely the case for global atmospheric models, let alone ESMs. Therefore, the high-resolution information of the SMAs has to be adapted to the coarser model grid before estimating the minerals' emission. If we assume that the heterogeneity of the local sources may be masked by the mixing of dust plumes at a regional scale (Scheuvens et al., 2013), the soil mineralogy at the coarser model resolution would correspond to the average of the high-resolution information from the soil maps. However, under the assumption that the mineralogy of the most abundant soil  
280 type is the one that determines the composition of a source, the dominant soil type over a grid cell provides a computationally efficient approach to derive the mineralogy at the model resolution, and it is the one currently implemented in MONARCH. The impact of this choice remains to be explored, and it may be significant in regions where the soil composition variability is high.

### 2.3.2 Deriving the emitted PSD of dust minerals from the soil composition

285 The mineralogy of the soils provided in the SMAs has been inferred in many cases via techniques that alter the original soil size distribution, i.e. through wet sieving. This dispersal is particularly relevant for the phyllosilicates, which are usually found in the form of aggregates in soils, and are detected in the atmosphere in higher proportions at coarser (silt) sizes than those reported in the soil maps (Perlwitz et al., 2015a; Pérez García-Pando et al., 2016). In these recent studies, it was also shown that Brittle Fragmentation Theory (BFT) (Kok, 2011) represents a practical framework to describe the emitted PSD in terms of  
290 its constituent minerals as it builds upon the dispersed soil PSD, which underpins the soil mineralogical datasets.

BFT is derived by analogy to the fragmentation of brittle materials such as glass spheres. It describes the emitted PSD as a power law between  $\sim 2$  and  $\sim 10 \mu\text{m}$  along with a depletion relative to his power law for dust  $> \sim 10 \mu\text{m}$ , depending on the side crack propagation length ( $\lambda$ ), and for dust  $< \sim 2 \mu\text{m}$  due to the size of the indivisible dust particles. In BFT the production of dust particles with sizes  $D_d$  is assumed to be proportional to the volume fraction of soil particles with sizes  $D_s \leq D_d$ . All in



295 all, the normalized emitted mass PSD can be expressed as:

$$\frac{dM_d}{d\ln D_d} = \frac{D_d}{C_m} \left[ 1 + \operatorname{erf} \left( \frac{\ln(D_d/\bar{D}_s)}{\sqrt{2}\ln(\sigma_s)} \right) \right] \exp \left[ - \left( \frac{D_d}{\lambda} \right)^3 \right]. \quad (1)$$

where  $\operatorname{erf}$  is the error function and  $C_m$  is a normalization constant. Kok (2011) assumed an invariant soil size distribution with a volume median diameter ( $\bar{D}_s$ ) of  $3.4 \pm 1.9 \mu\text{m}$  and a geometric standard deviation ( $\sigma_s$ ) of  $3.0 \pm 0.4$  derived from available measurements. With these values, a  $\lambda = 12 \pm 1 \mu\text{m}$  was obtained by fitting eq. 1 to measurements of the emitted size  
300 distribution.

Let  $m_{c_i}$  be the mass fraction of mineral  $i$  in the clay fraction, and  $m_{s_i}$  the mass fraction of mineral  $i$  in the silt fraction (see Appendix A). To derive the normalized mass size distribution for each emitted mineral we assume that aggregates are homogeneous mixtures of minerals with similar fragmentation properties. The emitted mass PSD for each mineral  $i$  (for each soil type and soil texture) can be derived as:

$$305 \quad \frac{dM_{d_i}}{d\ln D_d} = \frac{m_{c_i} D_d}{C_m} \left[ 1 + \operatorname{erf} \left( \frac{\ln(D_d/\bar{D}_s)}{\sqrt{2}\ln(\sigma_s)} \right) \right] \exp \left[ - \left( \frac{D_d}{\lambda} \right)^3 \right]; \quad \text{for } D_d \leq 2\mu\text{m} \quad (2)$$

$$\begin{aligned} \frac{dM_{d_i}}{d\ln D_d} = & \frac{m_{c_i} D_d}{C_m} \left[ 1 + \operatorname{erf} \left( \frac{\ln(2/\bar{D}_s)}{\sqrt{2}\ln(\sigma_s)} \right) \right] \exp \left[ - \left( \frac{D_d}{\lambda} \right)^3 \right] + \\ & \frac{m_{s_i} D_d}{C_m} \left[ \operatorname{erf} \left( \frac{\ln(D_d/\bar{D}_s)}{\sqrt{2}\ln(\sigma_s)} \right) - \operatorname{erf} \left( \frac{\ln(2/\bar{D}_s)}{\sqrt{2}\ln(\sigma_s)} \right) \right] \exp \left[ - \left( \frac{D_d}{\lambda} \right)^3 \right]; \quad \text{for } 2 < D_d \leq 20\mu\text{m} \end{aligned} \quad (3)$$

with  $\sum_i \frac{dM_{d_i}}{d\ln D_d} = \frac{dM_d}{d\ln D_d}$ . The emitted mass fraction  $M_{ik}$  of every mineral  $i$  in each size bin  $k$  relative to the total emitted mass up to  $20 \mu\text{m}$  is then estimated by integrating eq. 2 over each of the four smallest bins (i.e.,  $0.2\text{-}2 \mu\text{m}$ ) and eq. 3 over each of the four coarsest bins (i.e.,  $2\text{-}20 \mu\text{m}$ ):

$$310 \quad M_{ik} = \int_{D_{kmin}}^{D_{kmax}} \frac{dM_{d_i}}{d\ln D_d} \frac{1}{D_d} dD_d \quad (4)$$

with  $\sum_i \sum_k M_{ik} = 1$  and where  $D_{kmin}$  and  $D_{kmax}$  are the minimum and maximum diameters of each bin  $k$ .

Figure 1 compares the relative contribution of each mineral in each size bin in the soil and the emitted dust for one of the most abundant soil types in C1999-SMA. As expected from eq. 2 the minerals in the clay size range of the dispersed soil contribute exclusively and with the same proportion to the emitted particles below  $2 \mu\text{m}$ . Some of the silt-size aggregates are  
315 clay minerals (e.g. illite) that are disaggregated (or fragmented) during wet sieving and thus present at clay sizes in the SMA. For particle diameters above  $2 \mu\text{m}$ , the emitted mass of a given mineral has contributions from the dispersed soil clay and silt sizes as reflected in eq. 3. The redistribution of soil dispersed clay minerals into coarser emitted grains has a double effect: it includes phyllosilicates (e.g., illite, kaolinite, smectite) in these size ranges and reduces the fractional contribution of minerals originally reported in the silt sizes (e.g., quartz or feldspars), producing an aerosol size-resolved mineralogy more consistent  
320 with observations (Perlwitz et al., 2015b; Pérez García-Pando et al., 2016).

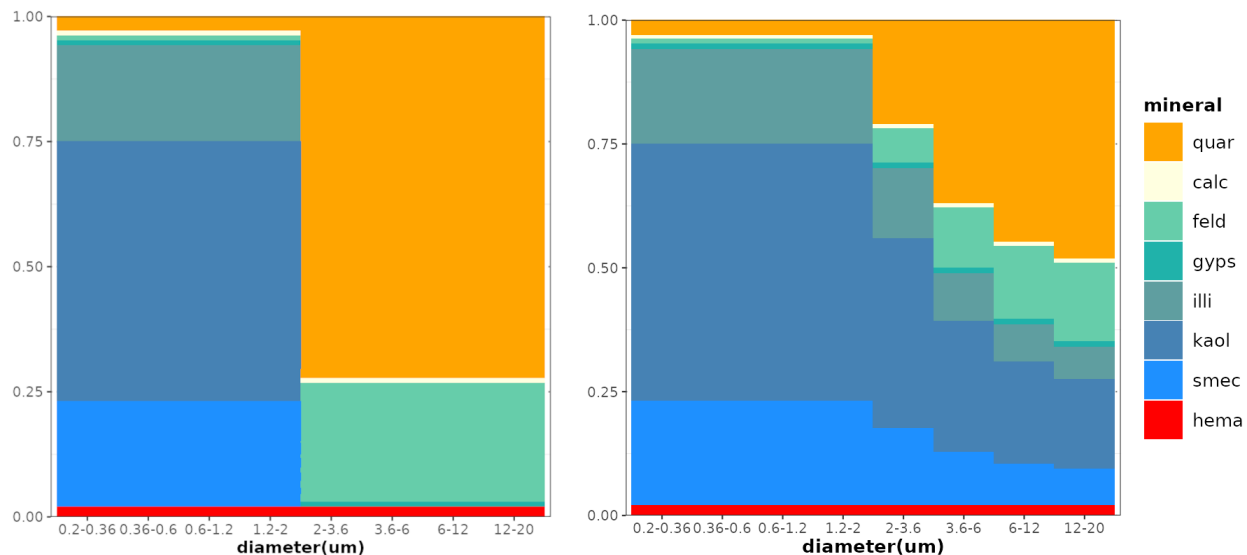


**Figure 1.** Normalized mass size distribution of minerals in the soil (left) and the aerosol (right) for the Xerosols Haplic soil type according to C1999-SMA. quar: quartz, calc: calcite, feld: feldspars, gyps: gypsum, illi: illite, kaol: kaolinite, smec: smectite, hema: hematite.

### 3 Experiments definition

We aim to assess the sensitivity of the ~~modelled~~modeled mineralogy and its potential climate impacts to the choice of a specific soil mineralogy. To that end, we design three different experiments (Table 2) that rely on the same model configuration and use the C1999-SMA, J2014-SMA normalized, and J2014-SMA non-normalized soil datasets described above (~~Section~~section 2.3.1); referred to as C1999, J2014 and J2014NN, respectively.

The configuration of MONARCH for the atmospheric physics is summarized in section 2.1, and the specific setup for the dust cycle in section 2.2. The simulations are performed at the global scale with a regular horizontal grid of 1°x1.4° (latitude x longitude) resolution and 48 vertical hybrid pressure-sigma layers up to 10 hPa. They cover the period from 2006 to 2010, after one year used as spin-up (2005) for the soil humidity and mineral initial conditions. The atmospheric meteorological variables are initialized from the ERA-Interim reanalysis (Berrisford et al., 2009; Dee et al., 2011) every 24 hours, to keep the ~~modelled~~modeled circulation close to observations and hence allow for a more precise comparison of the dust cycle to observations. ~~Soil~~However, the soil temperature and moisture, as well as ~~aerosol fields are recycled everyday~~the mineral dust fields, are those prognostically estimated by MONARCH (i.e., every day the model uses as initial state for these variables their modeled value at 24.00 h of the day before).

**Table 2.** Experiments definition.

Experiment	SMA	Description
C1999	C1999-SMA	8 minerals derived from Claquin et al. (1999) and Nickovic et al. (2012)
J2014	J2014-SMA	12 minerals derived from Journet et al. (2014), normalized to 100%
J2014NN	J2014-SMA	12 minerals derived from Journet et al. (2014), not normalized to 100% and an additional dust tracer of homogeneous composition

335 **4 Methodology and observational data for model evaluation**

**4.1 Dust observations and evaluation method**

MONARCH’s ability to reproduce the dust cycle with our selected configuration has been presented in Klose et al. (2021), who included an extensive evaluation of the dust optical properties compared to the AERosol RObotic NETwork (AERONET) (Holben et al., 1998; Giles et al., 2019) and MODIS (Ginoux et al., 2012; Hsu et al., 2013) retrievals. Here, we complement these  
340 previous analyses by including the composition-invariant dust in one of our experiments and assessing the ~~modelled~~modeled dust surface concentration and deposition fluxes against climatological observations. The purpose of these additional diagnostics is to provide a framework for the evaluation of the mineralogy, which ultimately depends on the ability of MONARCH to represent the atmospheric processes of the dust cycle.

We use the climatological observations of dust surface concentration from the Rosenstiel School of Marine and Atmospheric  
345 Science (RSMAS) of the University of Miami (Prospero, 1990; Arimoto et al., 1995; Prospero, 1996, 1999) and the African Monsoon Multidisciplinary Analysis (AMMA) international program (Marticorena et al., 2010), the latter from the French National Observatory Service International Network to study Deposition and Atmospheric composition in Africa (INDAAF; <https://indaaf.obs-mip.fr/>). The three AMMA sites provide measurements of surface dust concentration over North African sources below 10  $\mu\text{m}$  of diameter, while the 20 stations from the RSMAS are distributed over transport and remote regions  
350 (Figure 2a) and report total surface concentration. The dust evaluation is complemented through comparison with the dust deposition fluxes compiled by Albani et al. (2014) for present climate, which cover 110 locations (Figure 2a) and give also information on the fraction below 10  $\mu\text{m}$  in diameter. For the comparison, we compute the 5-year annual mean of ~~modelled~~modeled surface concentration and deposition fluxes of dust. For those measurements where the mass below 10  $\mu\text{m}$  in diameter is reported, we estimate the equivalent size range from the model. Spatially, the model values of the nearest neighbor cell to the  
355 observation location are taken. An overview of the model performance against each dataset is given through the estimates of the normalized Mean Bias (nMB), normalized Root Mean Square Error (nRMSE) and correlation (r). The definition of these metrics and their ranges of uncertainty can be found in ~~Section-section~~1 of the ~~Supplementary-materials~~Supplement.

## 4.2 Mineral observations and evaluation method

We conduct a direct evaluation of the ~~modelled~~modeled mineral fractions, both in surface concentrations and deposition fluxes, following Perlwitz et al. (2015b). That work compiles observed mineral mass fractions (%w) in surface concentration, along with total and dry deposition samples at 154 locations (Figure 2b), including data from single points and average information along ship-tracks. It details the number of samples taken, the standard deviation (when available), the sampling period, size range, location and reference to the original work from which the data are obtained. For ship campaigns, information about the ship initial and final locations is usually provided.

Most of the observational studies considered in Perlwitz et al. (2015b) tailor specifically dust, by methodology or by selection of dusty episodes. However, some of the observations may be affected by anthropogenic mineral contributions. Particularly, anthropogenic combustion processes and metal industry activities have been identified as a source of iron oxides, phyllosilicates or quartz particles (e.g., Querol et al., 1996; Rathod et al., 2020; Weinbruch et al., 2022). Our model estimates exclusively the mineralogy from natural dust sources, therefore we filter the observations in Perlwitz et al. (2015b) to remove those locations that could have an anthropogenic influence. To that end, we consider a multi-annual experiment conducted with the Community Atmosphere Model version 5 at the global scale (Hamilton et al., 2019), which accounts for mineral dust, biomass burning and anthropogenic sources of iron. We assume that mineralogy is dominated by dust in those areas where the ~~modelled~~annual mean contribution of iron from dust to the total iron concentration is of 75 % or larger (see ~~Section~~section 2 in the ~~Supplementary Materials~~Supplement). It has to be noted that the evaluation metrics using this filter are very close to those obtained using the full dataset (not shown), which suggests a small contribution of the anthropogenic sources in the studies selected by Perlwitz et al. (2015b).

The sampling periods range from specific days to multi-annual periods and span from the late 1960s to the 2000s. We consider the inter-annual variability of the mineral fractions to be relatively low (Perlwitz et al., 2015b). We assume that close to dust sources the mineralogy is mainly affected by the soil composition, which does not undergo substantial changes in the considered time period. During transport the mixing of dust plumes from different origins is expected to homogenize the dust composition, thus buffering the effect of an inter-annual change in each source strength. In summary, the observed values are compared with the ~~modelled~~modeled multi-annual means, even if they correspond to different time-periods. The sampling time and number of samples allow the derivation of an uncertainty range for the observed values, such that they can be compared with monthly ~~modelled~~modeled means (Perlwitz et al., 2015b). As the observations usually contain minerals that are not represented in this ~~modelling~~modeling study, we create a correspondence between the minerals reported and those ~~modelled~~modeled here and re-calculate the mass fractions and standard deviations of the observational data accordingly (see Table S1 and ~~Section~~section 2 in the ~~Supplementary Materials~~Supplement, for details).

The size distribution of the ~~modelled~~modeled minerals uses eight bins, with diameters from 0.2  $\mu\text{m}$  to 20  $\mu\text{m}$ . Observations are provided in different size ranges, including fractions lower than 2, 2.5, 4, 5, 10, 20, 30, 32, 40, 60, and 75  $\mu\text{m}$  in diameter, diameters between 1-2.5, 2.5-5, 2-20, 10-20, 20-32, 2-50, and 20-60  $\mu\text{m}$ , and bulk measurements. The observations with sizes entirely above our ~~modelled~~modeled size ranges (e.g., those reporting sizes from 20-40  $\mu\text{m}$  or 20-60  $\mu\text{m}$ ) are excluded from

our evaluation. We keep those observations that span larger diameters than the 20  $\mu\text{m}$  ~~modelled~~-modeled limit, but overlap with the ~~modelled~~-modeled size ranges (e.g., those reported as < 32  $\mu\text{m}$  or < 60  $\mu\text{m}$ ). For those observations below 20  $\mu\text{m}$ , we consider the specific observed size range and compute the equivalent model value, for the rest we compare the full model range, knowing that the size difference will introduce a bias in our comparison.

To summarize the evaluation, we aggregate the size ranges in 5 categories (Table 3): (1) below 2  $\mu\text{m}$ , and (2) between 2  $\mu\text{m}$  and 20  $\mu\text{m}$ , to assess if there is a difference in model performance for clay and silt size ranges; (3) below 10  $\mu\text{m}$  (to consider a size cut usually applied in air quality measurements), (4) below 20  $\mu\text{m}$  (to assess the full model size range), and (5) the bulk size (to include the observations that extend outside the model range).

We collocate temporally and spatially the ~~modelled~~-modeled and observed values. The temporal match is done on a monthly basis (e.g. if an observation reports values for January, the model corresponding value will be calculated as the mean of the January values for the 2006-2010 period). The spatial collocation is done by taking the nearest model cell to the location of the observation for fixed site measurements, and as an average of the cells nearest to the trajectory for the ship measurements.

In summary, the evaluation is performed collocating model and observations in terms of composition (we assess ratios only of minerals that are both ~~modelled~~-modeled and observed), size, location, and time (on a climatological monthly basis). From these pairs of observed and ~~modelled~~-modeled values we compute the nMB, nRMSE and r. In many occasions, the number of points available for our analyses is low, therefore we calculate the uncertainty ranges of these metrics at a 95% level, with the objective of more robustly assessing the significance of the differences among our experiments performance (See [Section section 1](#) in the Supplement, for details).

### 4.3 Diagnostic and evaluation of the minerals single scattering albedo

One of the key aspects that motivates the characterization of minerals within ESMs is the potential effect they have upon dust optical properties, and particularly the dust absorption at ultra-violet (UV) and visible (VIS) wavelengths. For that reason, we calculate offline the single scattering albedo (SSA) in the UV-VIS band (i.e. from 300 to 770 nm) that would result from the ~~modelled~~-modeled mineral mass concentrations in our two standard scenarios (C1999, J2014), and we compare them with an AERONET-derived climatology (2006-2010) of dust SSA in the same UV-VIS band (band averages are computed using optical depth and solar flux as weighting functions).

The calculation of mineral-dependent SSA in this contribution follows Obiso et al. (in prep.) and considers three externally-mixed mineral components: 1) externally mixed iron oxides, 2) all minerals other than iron oxides (host minerals) and 3) iron oxides internally mixed with host minerals (accretions). Each of these mineral components has a different refractive index, that we calculate by combining recent measurements of dust aerosols from natural parent soils (Di Biagio et al., 2017, 2019) and a collection of refractive indexes for individual minerals from Scanza et al. (2015). We estimate the refractive index of the mixture of host minerals by computing the volume-weighted mean of indexes from Scanza et al. (2015) based on the fractions of these minerals measured in soil samples by Di Biagio et al. (2017, 2019) (median among samples). For accretions, we take as a reference the 5 % by mass in the mixture that is imposed at emission to estimate the amount of internally mixed iron oxides (following Perlwitz et al., 2015b), and we directly use the refractive index retrieved by Di Biagio et al. (2019) for soil samples

with closest mass fractions of iron oxides (interpolation between 4.8 % and 5.8 %). Finally, for externally mixed iron oxides, we invert the empirical relationship (at different wavelengths) of imaginary index versus the soil content of iron oxides derived by Di Biagio et al. (2019) by fitting a Maxwell Garnett model to the observations (i.e., we estimate the imaginary index of iron oxides that would explain the observed relationship, using a value derived from Longtin et al. (1988) as the real index). The resulting refractive indices for these species are reported in section 3 of the Supplement.

To further assess the mineralogy effect upon the shortwave absorption, we also estimate the SSA that would result from applying dust homogeneous optical properties in the UV-VIS band, that are calculated using a globally uniform refractive index based on Sinyuk et al. (2003). In all these estimates, we use mass densities reported in Table 1 (averaging the values for iron oxides and host minerals in the calculation with three components) and consider dust particles to be spherical.

The AERONET version 3 level 2.0 Almucantar retrievals (Giles et al., 2019; Sinyuk et al., 2020) are filtered following the methodology in Obiso et al. (in prep.), that retains events dominated by dust, attempting to filter out the AERONET scenes contaminated by other absorbing aerosols (e.g. absorbing carbonaceous species). The hourly retrievals from AERONET are considered to represent dust when the fine volume fraction is small (below 15 %), the SSA increases from 440 nm to 675 nm (a feature that distinguishes dust from other species, see Dubovik et al., 2002), and the mean of the imaginary index at red and infra-red wavelengths (675, 870 and 1020 nm) is lower than 0.0042 (as higher values would indicate the presence of absorbing black and brown carbon, following Schuster et al., 2016). These criteria are applied to the available AERONET data for the 2006-2010 period, and monthly means over that period are computed only when 30 or more retrievals are available. Model monthly SSA are then interpolated at the selected AERONET stations (Figure 2a) and masked for unavailable months for the comparison with AERONET.

#### **4.4 Total iron from dust and evaluation**

Atmospheric deposition of soluble iron constitutes a key input of micro-nutrients to certain open ocean regions, where it can control primary productivity and thus carbon uptake (Jickells, 2005). Dust sources largely contribute to atmospheric iron emissions (e.g., Mahowald et al., 2009). However, the solubility of this emitted iron at origin is low and it is believed to increase through atmospheric processing. Both the amount of iron associated to dust and its susceptibility to becoming soluble in the atmosphere depend on mineralogy (Journet et al., 2008; Myriokefalitakis et al., 2018, 2022; Bergas-Massó et al., 2023). In section 6, we present an offline estimate of the total iron as derived from the mineralogy simulated in our experiments considering the iron content per mineral specified in Table 1. We assess the resulting surface concentration of total iron against climatological observations provided in Myriokefalitakis et al. (2018), filtered to avoid large contributions of combustion aerosols (either from anthropogenic or biomass burning origin) following the same criteria as for the mineralogy observations (see section 4.2 and Figure 1c). We also provide a proxy of the iron fractional solubility based on its mineralogical origin.



**Table 3.** Size classes considered for the evaluation of the mineral fractions and corresponding size ranges.

Size tag	Observation size ranges	Model sizes
< 2 $\mu\text{m}$	< 2 $\mu\text{m}$	same as observed
< 10 $\mu\text{m}$	<2.5, <4, <5, < 10 $\mu\text{m}$	same as observed
< 20 $\mu\text{m}$	< 20 $\mu\text{m}$	same as observed
2-20 $\mu\text{m}$	2.5-5, 5-10, 10-20, 2-20 $\mu\text{m}$	same as observed
bulk	< 30, <32, < 40, <60, <75, bulk	full range up to 20 $\mu\text{m}$ in diameter

## 5 Results and discussion

### 5.1 Evaluation of the dust cycle

With the current setup, and in line with Klose et al. (2021), MONARCH produces a total annual dust emission of  $3482.5 \pm 105.0$  Tg (mean  $\pm$  standard deviation of annual values over the 2006-2010 period) for particle diameters below 20  $\mu\text{m}$ . The annual mean atmospheric dust burden is of  $28.4 \pm 1.1$  Tg, and dry and wet deposition remove annually  $3394.7 \pm 104.1$  Tg from the atmosphere, with the former being the primary removal pathway ( $2019.4 \pm 79.3$  Tg  $\text{yr}^{-1}$ , compared to  $1375.3 \pm 26.6$  Tg  $\text{yr}^{-1}$ ). The annual average lifetime of dust in our experiments is then of  $3.05 \pm 0.04$  days. These values fall within the range of recent multi-model estimates constrained by observations (Kok et al., 2021). Our current implementation accounts for the effect of the density and size distribution of the different minerals in the transport and deposition processes, however, these alone do not substantially change the dust cycle (when we sum the minerals mass as compared to the compositionally homogeneous dust tracer).

Major dust sources are represented over the Northern Hemisphere desert belt (Figure 3a). As a result, high annual mean surface concentrations are ~~modelled~~modeled over North Africa and East Asian regions (Figure 3b), which present a relatively fair agreement with observations (model estimates fall within the range of two-times the observational value for most of the sites in these regions, Figure 4a). The Atlantic transport is well captured by the model, and leads to annual mean surface concentrations over central America close to the observations. This is also the case for the ~~modelled~~modeled surface dust concentration over the North Pacific (Figure 4a). Dust in the Southern Hemisphere is primarily emitted from South America, Australia, and to a less extent South African sources (Figure 3a). The model tends to misrepresent the observed dust surface concentration at Southern Hemisphere locations (e.g., over Australian or South Pacific sites ~~modelled~~modeled values fall only within one order of magnitude of the observations), with an overall underestimation that seems particularly relevant for remote stations (e.g., those over the Southern Ocean). Other global models (Albani et al., 2014; Checa-Garcia et al., 2021) show similar or worse performances in representing the dust surface concentration in the Southern Ocean, with deviations from the observations of one order of magnitude. Globally, MONARCH slightly overestimates the surface concentration (nMB of 12.5 %). The deviation from observations (nRMSE of 116.0%) is largely influenced by the aforementioned poor representation of the Southern Hemisphere surface concentration levels. In spite of these biases, MONARCH reproduces the dust surface

concentration spatial variations as described by the observations, with a correlation towards worldwide observations of 0.95 when the 23 measurement locations are considered (Figure 4a, Table [S2-S3](#) in the Supplement summarizes the evaluation statistics).

The dust deposition fluxes (Figure 3c) are overall underestimated by the model, and errors are larger than for the surface concentration field (nMB=-57.3 %, nRMSE=210.7 %, as an average over all measurement points; Figure 4b; Table [S2-S3](#) in the Supplement). Most of the ~~modelled~~modeled deposition fluxes fall within one order of magnitude of the observations, although the model behaviour is particularly poor in some locations of the North and South Pacific, and Australian regions, with underestimations beyond that (Figure 4b). MONARCH estimates are the closest to the observations for some points over sources (e.g., some locations over North Africa), but also some over remote regions (e.g., the Southern Ocean), which points to multiple causes for the differences with respect to observations. Over sources, gravitational settling dominates the deposition flux and the fraction of coarse particles present plays a relevant role in the deposited mass. In transport or remote regions, the finest dust fractions dominate and removal is controlled primarily by wet deposition processes (Huneus et al., 2011; Kok et al., 2021). The geographical variability of the deposition is acceptably captured by the model, showing a correlation of 0.80 over the 110 measurement considered. Overall, MONARCH shows similar skills in representing dust deposition than other global atmospheric models (Huneus et al., 2011; Albani et al., 2014; Checa-Garcia et al., 2021).

## 5.2 ~~Modelled~~Modeled mineralogy at emission

The choice of the soil composition map, and the approach used to represent it in the model, has a direct influence on the emitted mineral fractions (Figure 5, Table 4).

Within our ~~modelled~~modeled size range (up to 20  $\mu\text{m}$  in diameter), quartz is the most abundant mineral at emission, regardless of the soil mineralogy selected. On an annual basis, J2014 (J2014NN) yields a lower global fractional mass for quartz over sources than C1999, but both experiments reflect this mineral's ubiquity, accounting for 39.0 %, and 31.7 % (28.1 %) of the global emission budget in C1999 and J2014 (J2014NN), respectively. Regionally, the quartz contribution can be higher, being up to 42.2 % of the total annual emitted dust over East Asian sources in the C1999 experiment.

Phyllosilicate minerals, when added together (illite, kaolinite and smectite in C1999, plus chlorite, vermiculite and mica in J2014 (J2014NN)), are also substantial over sources, and make up a significant fraction of the emitted dust (39.8 % and 47.1 % (43.1 %) in C1999 and J2014 (J2014NN) at the global scale, respectively). C1999 reflects a higher kaolinite to illite ratio over the Sahel, than over northern African regions, likely associated to the more weathered soils (Scheuven et al., 2013), however this signature does not appear in J2014 (J2014NN). The largest differences between C1999 and J2014 (J2014NN) occur over Australian sources: in J2014 and J2014NN, kaolinite dominates compared to illite and smectite, while in C1999 higher fractions of smectite are present, balanced with kaolinite and illite. The impact of adding vermiculite, chlorite and mica in J2014 (J2014NN) is relatively low, as their contribution to the total emitted dust is estimated at 11.4 % (10.7 %), globally.

Overall, C1999 emits a higher mass fraction of feldspars than J2014 (J2014NN), 13.0 %, compared to 10.8 % (9.7 %), globally, and differences are particularly large for specific sources, such as Australia, where the C1999 emitted feldspars fraction doubles that in J2014 (J2014NN), 24.4 %, compared to 11.3 % (10.7 %).

515 Calcite is less abundant in C1999 emission, 5.2 %, than in J2014 (J2014NN), 8.4 % (7.4 %), although both experiments share regional variability. The large carbonate fraction associated to North African soils and attributed to the underlying geology (Formenti et al., 2011; Scheuvens et al., 2013) is reflected both in C1999 and J2014 (J2014NN) with higher calcite fractions over west and east North Africa than in the Sahel area. Also in both maps, Middle Eastern and Central Asian sources are the richest in calcite. Over the Southern Hemisphere sources (e.g. South American, or South African sources), there is less  
520 agreement between experiments.

The largest differences in emitted fractions at the global scale are for iron oxides, where C1999 originally considers only hematite, yielding 1.6 % of the total emitted dust mass, J2014 (J2014NN) augment hematite with goethite, with 0.6 % (0.5 %) and 1.4 % (1.3 %) contributions to the total emitted dust, respectively. Due to the high sensitivity of dust radiation absorption to the abundance of iron oxides, these relatively small differences at emission have a relevant impact on the estimates of  
525 dust optical properties, as it will be discussed in ~~Section~~section 6. Regionally, C1999 produces a higher emitted fraction of iron oxides over the Sahel region than in northern areas of North Africa. In contrast, J2014 (J2014NN) yields a higher fractional emission of iron oxides over East and West North Africa than over the Sahel area. For these relevant dust sources, the regional variability produced by C1999 may align better with observational evidences (Formenti et al., 2008, 2014). Despite the differences at global and regional scale, both experiments point to Australian sources being rich in iron oxides (either hematite  
530 in C1999 or hematite and goethite in J2014 (J2014NN)), compared to other regions.

Gypsum is a minor component of the emitted dust, amounting globally 1.4 % in C1999, and one order of magnitude less, 0.1 %, in J2014 (J2014NN). Note that the original Journet et al. (2014) work does not explicitly report this mineral, and its estimation comes from the data compiled in the HWSDv1.1.

Regionally, we find that overall C1999 shows a larger variability among sources than J2014 or J2014NN for quartz and  
535 feldspar, while the fractions of calcite, phyllosilicates, and iron oxides vary more among regions in J2014 (J2014NN). In spite of the higher resolution of the original Journet et al. (2014) dataset, the variability in quartz and feldspars is masked by the effect of the multiple assumptions required to fill in the silt fraction data in soils, which in many occasions involve averaging over the composition of multiple soil units.

If we consider J2014NN, at the global scale, the total undetermined mineral fraction at emission adds up to a 9.8 %, a non-  
540 negligible fraction. This assumption leads to relative differences in the emitted mineral mass that range from 3.8% for hematite, to up to a 25.8 % for gypsum compared to J2014 (Table 4). For the Sahel, Australia or East North Africa, the unknown fraction is lower than at global scale ( $\approx 7$  to 8 %), while in Central and East Asia, or North America is higher ( $\approx 14$  to 16 %). This variability among regions does not lead to substantial changes in the ratios among known minerals, that is, if we re-calculate the mineral emitted fractions for J2014NN considering that dust is made of our identifiable minerals, the resulting mass fractions  
545 are close to those obtained from the J2014 experiment (with differences up to 0.6 %). However, it suggests that for some regions the ~~modelled~~modeled minerals do not fully represent the dust composition.

### 5.3 ~~Modelled~~Modeled mineralogy in the atmosphere and at deposition

At the global scale, coarse minerals such as quartz, feldspars or even calcite preferentially reduce their abundance once in the atmosphere with respect to emission (Table 4). In contrast, the mass fractions of finer minerals (i.e., illite, kaolinite, smectite, or vermiculite) increase compared to their emitted fractions. Both quartz and feldspar have lifetimes around 2.7 or 2.8 days depending on the experiment, lower than those of dust with mean composition. The atmospheric lifetimes of calcite differ between C1999, 2.7 days, and J2014 (J2014NN), 3.0 days, which is attributed to the different size distributions of this mineral in the two soil datasets. Overall, clay minerals remain longer in the atmosphere than homogeneous dust (with lifetimes above 3.0 days).

Although dry deposition is the predominant removal pathway for all minerals, the deposited mass fraction of the coarser and denser minerals (quartz, feldspar, calcite) is higher in dry deposition than in wet deposition, while finer clay minerals (illite, smectite, kaolinite, vermiculite, chlorite) that remain longer in the atmosphere, increase their deposited fractions in wet deposition compared to dry deposition.

In our ~~modelling~~modeling framework, we assume that a large fraction of iron oxides at emission is internally mixed with phyllosilicates, and therefore is transported and deposited as such. As a result, the lifetimes of iron oxides (C1999), hematite, or goethite (J2014, J2014NN) follow the same trend as those of typical clay minerals, with slightly larger abundances in the atmosphere than at emission, a larger mass fraction at wet deposition than at dry deposition, and overall longer lifetimes than homogeneous dust.

There are no substantial changes in the residence times of the ~~modelled~~modeled minerals between J2014 and J2014NN, suggesting that the normalization of the 12 minerals from J2014 does not substantially modify their size distribution and relative abundances. Given that the relative mass fractions at emission and deposition when we consider exclusively the twelve known minerals are also close, for now on we will focus our discussion on the comparison between C1999 and J2014 experiments.

#### 5.3.1 Phyllosilicates

The mass fraction of the ~~modelled~~modeled phyllosilicates at the surface is overall lower over source regions (ranging from ~30 to ~50 % in total) than at remote or transport regions, where dust is enriched in clay minerals (up to ~ 80 %), due to the preferential deposition of coarser and denser minerals close to sources (Figure 6).

Both C1999 and J2014 show similar geographical patterns and contribution to total dust mass at the surface of clay phyllosilicates (i.e. illite, kaolinite and smectite, in C1999, plus vermiculite and chlorite, in J2014), with differences below ~10 % mainly in plumes from Southern Hemisphere sources (e.g. Australia, South Africa or South American sources), East Asia or the Bodélé in North Africa. Differences between experiments increase when the different phyllosilicates are assessed independently, with overall lower (higher) mass fractions of illite (kaolinite) at the surface from North African, North America and Australian sources, and higher (lower) mass fractions from North West Africa, the Bodélé and South American sources, in J2014 compared to C1999. The smectite mass fraction at the surface is overall lower in J2014 with respect to C1999, particularly in the Southern Hemisphere (Figure 6e,f). Mica is a phyllosilicate of the same group as illite, but allocated in the soil map

580 from J2014 to coarser sizes. If we add mica to the comparison, J2014 provides a higher mass fraction of total phyllosilicates in most dust sources (up to 15 %, see Figure [S2-S3](#) in the Supplement).

C1999 seems to reproduce better the observed geographical distribution of phyllosilicate minerals, particularly illite and smectite, than J2014 (size-dependent spatial correlation above 0.37 and below 0.26, respectively), but also for kaolinite (with higher correlation 0.67 vs. 0.47, and lower nRMSE and nMB). Overall, there is a general overestimation of the kaolinite and  
585 smectite fractions, while an underestimation of the illite (Figure 7). In the finer clay size range (below 2  $\mu\text{m}$ ), both C1999 and J2014 overestimate the illite mass fraction close to sources and underestimate it in transport or remote regions, while the coarser silt-sized fractions are overall underestimated (i.e. close and far from sources, Figure 7). The latter may be caused by a still insufficient re-distribution of soil clay mineral fractions towards coarser emitted sizes, even after applying the BFT.

### 5.3.2 Quartz, feldspars and calcite

590 According to C1999, quartz makes up a large fraction of the dust surface concentration over major dust sources (up to  $\sim 50$  %), which is explained both by its high mass fraction at emission and also to the preferential removal close to sources, due to its size and density. J2014 produces slightly lower mass fractions of quartz over the Northern Hemisphere, particularly over North African and Asian sources ( $\sim 10 - 15$  % lower), and slightly higher fractions over Australian sources ( $\sim 10 - 15$  %, Figure 8).

595 The feldspar mass fraction also peaks over sources, with a contribution in C1999 of up to  $\sim 25\%$  of the total dust in specific regions, particularly over Australia (up to  $\sim 25$  %), where in J2014 it is reduced by  $\sim 15 - 20$  % (Figure 8).

The calcite contribution to the surface is largest over Asian and South African sources in C1999 (making up to  $\sim 15\%$  of the dust mass), with relatively low mass fractions within the Atlantic dust plume (originated in North Africa) and from South American sources (Figure 8). Overall, J2014 shows higher calcite mass fractions (up to  $\sim 15$  %), except for some Southern  
600 Hemisphere regions (e.g. Australia and South Africa) and some spots over Asia, where calcite is less abundant than in C1999 (Figure 8).

MONARCH tends to overestimate the silt-sized fraction of quartz (Figure 9), and underestimate the clay-sized fraction, independently of the soil map. The model is unable to capture the size and spatial variability of this mineral as described by observations. Similar to illite, we think that these discrepancies are due to the excessive allocation of quartz to the coarser  
605 sizes that is derived from the soil information. Even after re-distribution of other emitted minerals to silt sizes through BFT, an excessive mass fraction of quartz is projected in the coarsest silt transport bins, leading to the overestimation shown in particles with diameters below 10  $\mu\text{m}$  and between 2 and 20  $\mu\text{m}$ . The excellent agreement of the ~~modelled~~-modeled quartz fraction with observed fractions in the bulk sized particles reinforces this hypothesis. The observed quartz fraction normally increases with particle size. When we compare our ~~modelled~~-modeled size range, up to 20  $\mu\text{m}$ , with observed quartz fraction in particles  
610 larger than that, there is an artificial reduction in bias.

All our estimates rely in relative mass fractions, therefore the quartz overestimation in the silt sizes could be the reason explaining the underestimation of other typically coarse minerals, such as feldspar (Figure 9). Overall, J2014 shows less variability in the ~~modelled~~-modeled feldspar fraction than C1999, something we attribute to the multiple assumptions that

Journet et al. (2014) made in order to fill in the missing information on the silt sizes, which many times involved averaging mass fractions over multiple soil categories (see [Figures S2 and S4](#) [Figure S9](#) in the Supplement). Despite the low variability, the size-dependent spatial correlation of the model versus observations is larger in J2014 than in C1999, although with larger errors and biases. It has to be noted here that the original J2014-SMA includes feldspar both in the clay and silt soil sizes, while we artificially introduce the feldspars clay fraction in C1999-SMA using the available information in the silt sizes (see section A2 in Appendix A, for details).

Calcite is slightly underestimated in the C1999 experiment, particularly for the 2-20  $\mu\text{m}$  size range (Figure 9); therefore the increased mass fractions obtained with J2014 produce more realistic levels when compared to observations. In many cases, calcite size apportionment has been inferred from soil texture data in the original soil maps. Both C1999 and J2014 poorly represent the size-dependent spatial distribution of this mineral, as shown by the low correlation in Figure 9.

### 5.3.3 Iron oxides

Iron oxides, represented as hematite in C1999, and as the sum of hematite and goethite in J2014, constitute a small fraction of the total dust load (Figure 10). At the surface, mass fractions up to  $\sim 3.5\%$  occur in dust plumes from the Bodélé, the Sahel and Northwest African sources, as well as in some areas of the Middle East and North America in our C1999 experiment. Also, Australian dust is rich in iron oxides, with contributions up to  $\sim 4\%$ , that influence the delivery of iron to the South Pacific region (e.g., [Bergas-Massó et al. \(2023\)](#)). J2014-SMA follows current evidence (Lafon et al., 2006; Formenti et al., 2008) of goethite being more abundant in soils than hematite, and this is reflected in the aerosol abundance.

The hematite levels in J2014 are lower than those in C1999 (up to  $\sim 3\%$ ), particularly over those regions where the maximum mass fractions in the surface concentration are shown. Considering the sum of hematite and goethite, J2014 provides an overall higher mass fraction of iron oxides at the surface than C1999 (differences up to  $\sim 5\%$  over Australian sources). However, dust plumes originating in the Sahel and the Bodélé areas have lower iron oxides content in J2014 than in C1999 (Figure 10). These constitute relevant dust sources and while observational evidences (Formenti et al., 2008; Go et al., 2022) support the Bodélé being depleted in iron oxides, they also suggest that the Sahel (characterized by intense soil weathering) is rich in iron oxides, a feature that would be better captured by C1999.

The available observations of hematite mass fractions are from two observation sites, one in Izaña (Tenerife, Spain) and the other in Tinfou (Morocco) (Kandler et al., 2007, 2009). For these spots, located or influenced by African sources, [both C1999 slightly underestimates and J2014 underestimate](#) the hematite content, [and it shows a lower error with observations however C1999 shows a slightly lower error and higher correlation](#) than J2014, [while J2014 overestimates the measurements at those locations \(Figure 11a \(Figure 11a and c\)\)](#). This comparison potentially supports the more realistic geographical distribution of iron oxides over North Africa in C1999, although the number of observations is [too](#) low to extract sound conclusions (differences in the evaluation metrics are not statistically significant). When we consider iron oxides, the number of observation sites increases. Please, note that measurements reporting iron oxides do not necessarily report on goethite and hematite, but they could be referring exclusively to hematite. Overall, J2014 provides a better agreement with the spatial and size distribution of the observations than C1999 (higher correlation) and similar errors. These results suggest that the introduction of goethite



has a positive impact on estimating the total iron oxides content, which is generally underestimated in C1999. It is yet to be determined if this is related to the iron oxides speciation, their geographical distribution or just the increased mass fractions.

650 More observations are needed and are very much desirable to be able to discuss their abundances and how they impact dust optical properties or ocean biogeochemistry.

## 6 Implications of modelled-modeled mineralogy for dust-climate interactions

The abundance of iron oxides determines the radiation absorption by mineral dust in the SW, the higher the amount of iron oxides, the lower the single scattering albedo. Our offline calculations of SSA in the UV-VIS band ( $0.3 - 0.77 \mu m$ ) for a dust of homogeneous composition range from 0.919 to 0.966 at the annual scale (Figure 12a). When we consider the mineralogy variations, the annual mean SSA scales with the abundance of iron oxides, with lowest values in C1999 ( $\sim 0.899$ ) over Australia, and slightly absorbing features in the dust plumes from the Bodélé, the Sahel, the Middle East and South American sources ( $\sim 0.92$ ) (Figure 12b). Transport or remote regions are characterized by more scattering dust mixtures, with SSA up to 0.972. In line with the higher iron oxides content (see [Section-section 5.3.3](#)), the mineralogy of J2014 shows overall more absorbing features (with differences in SSA of  $\sim 4 \%$  over Australia,  $\sim 0.856$ , Figure 12c), except for the dust plume originating at the Bódélé depression, where J2014 shows lower iron oxide abundances and hence slightly more scattering dust properties. Our off-line calculated SSA regional variations, from 0.899 to 0.972 in C1999, and from 0.856 to 0.960 in J2014, reach more absorbing values than the mineral-dependent estimates of Journet et al. (2014), which ranged at visible wavelengths from 0.935 to 0.975, using a core and shell model to estimate the optical properties. On the other hand, our estimates show more scattering features than those in Li et al. (2021). Their SSA in the  $0.44 - 0.63 \mu m$  band ranges from 0.83 to 0.93 over dusty regions. The differences with our estimates are attributed both to the broader range of iron oxides abundance in their study, due to the use of the uncertainty ranges in the soil maps, and to the calculation of the dust complex refractive index through the minerals' volume average, which may overestimate the absorption.

660

Our SSA calculation assuming regionally homogeneous dust optical properties that are independent of mineral content produces a lower spatio-temporal variability with respect to dust-filtered AERONET retrievals in the selected stations and months (Figure 12d), with a monthly SSA standard deviation of 0.005 compared to 0.011. The introduction of mineralogical variations according to C1999 (J2014), Figure 12e (f), increases this variability and brings it closer to the observed range, with a standard deviation of 0.007 (0.008). Despite the existing uncertainties on the characterization of iron oxides, reflected in the poor correlations with AERONET retrievals in all cases, considering the regionally varying composition has a positive impact in our comparison with AERONET and thus represents a first promising step towards a more realistic representation of dust absorption and its climate impact.

670

~~Atmospheric deposition of soluble iron constitutes a key input of micro-nutrients to certain open ocean regions, where it can control primary productivity and thus carbon uptake (Jickells, 2005). Dust sources largely contribute to atmospheric iron emissions. However, the solubility of this emitted iron at origin is low and it is believed to increase through atmospheric~~

680 processing. Both the amount of iron associated to dust and its susceptibility to becoming soluble in the atmosphere depend on the mineralogy (Journet et al., 2008; Myriokefalitakis et al., 2022; ?).

On the other hand, dust is known to be a major source of iron to the atmosphere, which is relevant for ocean biogeochemistry upon deposition. The choice of a specific soil map has a large impact on the total iron estimates (Figure 12a and b). The C1999 experiment emits  $70.23 \text{ Tg yr}^{-1}$  of iron on average for 2006-2010, which globally represents a 2.0 w% of the total dust emitted mass, while J2014 derives in  $97.64 \text{ Tg yr}^{-1}$ , a 2.8 w% of the total dust emission. Both. In J2014NN, as we account for the fraction of dust with an unknown composition, to which we do not attribute any iron content, thus the total iron emitted adds up to  $89.5 \text{ Tg yr}^{-1}$  (i.e., 2.6 w% of dust). All of them fall below the 3.5 w% iron-to-dust ratio commonly assumed in modelling-modeling studies that do not resolve dust mineralogy (e.g., Luo et al., 2008; Mahowald et al., 2009) (e.g., Luo et al., 2008; Mahowald et al., 2009; Ito and Xu, 2014). Mineralogy resolving models produce higher iron-to-dust ratios when they represent smaller size ranges than MONARCH (e.g., Scanza et al. 2018, three of the models in Myriokefalitakis et al. 2018 or Wang et al. 2015 emit dust up to 10  $\mu\text{m}$  in diameter with 3.2 to 4.6w% of iron). Models sharing similar size ranges (e.g., the IMPACT model in Myriokefalitakis et al. 2018 traces dust particles up to 20  $\mu\text{m}$  in diameter) result in similar mass ratios (i.e., 2.65w%). This enrichment in small size ranges is attributed to the high abundance of phyllosilicates with large structural iron content (see Table 1). Finally, the use of J2014 (or J2014NN) yields high iron at emission for comparable size ranges due to the contribution of iron-rich minerals (i.e., chlorite and vermiculite) which are not represented in C1999, and also to the higher illite and smectite mass fractions in J2014.

The comparison of our diagnosed total iron with surface concentration observations suggests that C1999 underestimates the elemental iron present in dust. As a result of the higher iron-to-dust ratios, this bias is slightly reduced when we consider J2014NN (see section 7 in the Supplement) and gets closer to zero with J2014 on average. On the contrary, applying a constant 3.5w% of iron in dust would lead to an overestimation of the observed total iron surface concentration (Figure 13). The spatio-temporal variability of the modeled iron is primarily driven by the ability of the model to derive the dust fields, for that reason, the correlation of the diagnosed iron surface concentration is close in all the experiments and in the case of the homogeneous dust.

In line with the emission, overall, globally the amount of total iron deposited in J2014 (and J2014NN) is larger than in C1999, with 95.0 ( $1387.0 \text{ Tg yr}^{-1}$ ) (Figure 14a and b), particularly over the Atlantic and Indian oceans. These differences are mostly attributed to phyllosilicates, as J2014 include two iron-enriched clay minerals (vermiculite and chlorite) that are not present, and section 7 of the Supplement). In all experiments, dry deposition is the predominant removal process (representing 57% and 58% of the total iron deposition in C1999 and J2014, respectively). These estimates fall within those reported in previous modeling studies ( $71.5 \pm 43 \text{ Tg yr}^{-1}$ ) applying both C1999 and J2014NN (Myriokefalitakis et al., 2018), which also highlights the relevance of dry deposition for dust-originated iron removal. Regionally, the largest differences in total iron deposition between C1999 and J2014 occur over the Atlantic and Indian oceans, while over the Southern Ocean (and in general the Southern Hemisphere basins), both soil mineralogy maps yield similarly low total iron deposition fluxes, which may be due to a general underestimation of dust deposition in our model.

over. Our model tends to underestimate the total deposited dust mass in this region (Section 5.1)see Figure 4 and Table S03 in the Supplement), which has a direct impact on the estimated total iron deposition fluxes.

Evidence suggests that a small fraction of the iron, present in amorphous and poorly crystalline minerals in the form of ferrihydrite and nano-iron oxides, is soluble and highly reactive. Structural iron, embedded in phyllosilicate matrices, is usually considered as more difficult to dissolve, while iron in larger crystalline iron oxide particles (e.g., hematite or goethite) is the most refractory fraction (Shi et al., 2011, 2012; Ito and Xu, 2014). The representation of atmospheric iron dissolution through acidic processing as a 3-stage kinetic mechanism (Shi et al., 2011) has been adopted by different atmospheric models (e.g., Myriokefalitakis et al., 2015; Ito and Xu, 2014; Ito and Shi, 2016; Seanza et al., 2018; Myriokefalitakis et al., 2022; ?) (e.g., Myriokefalitakis et al., 2015; Ito and Xu, 2014; Ito and Shi, 2016; Seanza et al., 2018; Myriokefalitakis et al., 2022; ?), which usually partition the total emitted iron into different dissolution pools. In lack of better estimates, the amount of iron in ferrihydrite and nano-iron oxides, which dissolves fast (FeF), is usually computed as a small fraction of the total iron (e.g., Ito and Shi, 2016; Myriokefalitakis et al., 2022; ?) (e.g., Ito and Shi, 2016; Myriokefalitakis et al., 2022; Bergas-Massó et al., 2023), in line with observational evidence (Shi et al., 2012).

The ratio of poorly, FeF, to highly crystalline iron oxides (FeOx) can be used as a measure of the susceptibility of iron to dissolve, but also to characterize the ageing of iron oxides (Shi et al., 2012). Usually, more weathered soils show lower ratios of more reactive iron species, as they are easily transformed into more stable forms. Over North Africa, the C1999 experiment shows more ageing for the Sahel region, i.e., lower fraction of highly reactive (FeF) over crystalline iron oxides (FeOx) and potentially lower solubility, while in J2014 the contrast between the Sahara and the Sahel areas is less visible (Figure 13 and 14c and d). In J2014, the Bodelé depression is characterized by a high FeF / FeOx ratio. Both features are consistent with observations (Shi et al., 2012) and in line with our previous analyses on the crystalline iron oxides (Section 5.3.3).

In addition to the susceptibility of iron dissolution owed to its morphology, the acidity of the aerosols is a key factor controlling the solubilization process (Journet et al., 2008; Myriokefalitakis et al., 2022; ?)(Journet et al., 2008; Myriokefalitakis et al., 2022; Ber . Alkaline compounds in dust (such as calcite) can act as buffering species for acidic conditions. The higher levels of calcite in J2014 (Figure 8) could potentially result in more basic aerosol pH, and a reduced solubilization of iron through acidic attack.

## 7 Conclusions

Representing the mineralogy of atmospheric dust in Earth System Models requires information on the size-resolved composition of the uppermost layer of the parent soils. This work examines three variations of currently available soil mineralogy maps in a set of otherwise identical ~~modelling~~modeling experiments. Our reference maps are the C1999-SMA, from Claquin et al. (1999) and Nickovic et al. (2012), and two variations of the J2014-SMA, Journet et al. (2014). These maps constitute our best knowledge to date of the parent soils' composition at a global scale, even though they are derived by extrapolation of a scarce set of soil mineralogy observations, and thus present large uncertainties. Despite these uncertainties, we show here that they share some common robust properties. For our ~~modelled~~modeled dust size range (up to 20  $\mu\text{m}$  of diameter), quartz is consistently the most abundant mineral (%w) at emission, independently of the source region and soil map used. Also, the phyllosilicates (illite, kaolinite, smectite, with C1999-SMA, plus vermiculite, chlorite and mica with J2014-SMA)

show a similar distribution amongst our experiments. Globally, illite is more abundant than kaolinite, and than smectite. The largest uncertainties are related to less abundant minerals, such as feldspars, calcite, and particularly the iron oxides. One of the variants of the J2014-SMA map considers the raw mineralogical information provided by the soil observations, without  
750 normalizing their relative contributions to constitute the whole emitted dust mass. Using that information, we assess that at the global scale almost a 10% of the total emitted dust has an undetermined composition. The unknown fraction can be regionally higher, suggesting that in some areas our knowledge of the composition of dust sources is more robust than in others.

The emitted size distribution of the minerals is a key factor controlling their geographical distribution and lifetimes. Coarse-grained minerals, such as quartz, feldspars or calcite, are preferentially removed from the atmosphere by gravitational settling,  
755 hence showing higher abundances close to sources. In contrast, smaller clay-sized phyllosilicates remain longer in the atmosphere and constitute a large fraction of the dust transported to remote regions. The current SMAs provide a crude estimate of the soil size distribution for each mineral, distinguishing exclusively between the clay and silt size classes. In addition, the analyses applied on the soil samples often result in a disaggregation of soil aggregates that is much more intense than that caused by wind erosion, therefore overemphasizing the abundance of fine phyllosilicate fractions in soils compared to their  
760 presence in equivalent aerosol sizes. By applying Brittle Fragmentation Theory (BFT) to derive the emitted size distribution for each mineral, we partially overcome this issue. BFT restores phyllosilicates at coarser sizes and reduces at the same time the mass fractions of typically coarse minerals. Even with this re-aggregation, in all our experiments, the model overestimates the observed quartz mass fractions at coarse sizes, and underestimates those in the finer ones (below 2  $\mu\text{m}$ ). This ~~suggests that an excessive quartz fraction is still apportioned in the silt-sized emissions, hence inducing underestimations of~~ bias is attributed to the poor representation of the minerals' size distribution in the soils, which neglects the increased abundance of quartz with size. The SMAs provide a constant quartz proportion for soil grains from 2 up to 63  $\mu\text{m}$  in diameter, which is likely too large for the smaller silt particles. As a consequence of the overestimation of the relative fraction of quartz, the model underestimates  
765 other typically coarse minerals over the same size ranges, e.g., feldspars. Further extensions of BFT are planned, particularly in the description of the soil mineral size distributions, which we expect it will yield a more realistic size distribution of the  
770 emitted minerals.

The comparison with observations suggests that C1999 represents best the phyllosilicates. Particularly, kaolinite, which is also qualitatively in agreement with the expected distribution in soils, i.e., higher mass fractions correspond to regions of intense weathering. Feldspar abundance shows a larger spatial variability and slightly lower errors with C1999-SMA; we attribute this to the particularly sparse information for the silt size fraction in J2014-SMA, which required extensions in many cases through  
775 the use of averages over multiple soil classes. However, the size apportionment in C1999-SMA excluded feldspars from the finer soil fractions, which results in a poor correlation with observations in size and space. Calcite levels are overall better reproduced with J2014-SMA, with large underestimations in C1999. Both maps represent qualitatively known variations of calcite in North African soils (with higher mass fractions over the Sahara than in the Sahel).

The available observations of iron oxides are scarce, and do not allow for a comprehensive assessment, however the iron  
780 oxides apportionment provided in J2014-SMA seems to be in better agreement with recent evidences than the C1999-SMA database. A majority of observations suggest that goethite is more abundant than hematite in soils and that the latter is usually

confined to the smaller sizes, whereas goethite appears both in fine and coarse fractions. Also, if hematite with C1999-SMA, and hematite plus goethite with J2014-SMA, are both compared to observations of total iron oxides, the latter provides slightly better correlation in size and space. Over relevant North African dust sources, the regional variations described by the two  
785 soil maps differ, and while C1999-SMA represents better the higher iron oxides' content of the weathered Sahelian soils, J2014-SMA identifies the Bódélé depression as depleted in iron oxides, both features consistent with observational evidence.

The iron oxides abundance is directly associated with the dust absorption properties in the SW, and therefore our estimates of dust SSA in the UV-VIS band are impacted by the choice of the soil map. Despite the poor spatio-temporal correlation with AERONET-derived SSA, likely due to inaccuracies in the current prescription of iron oxides' soil content, considering  
790 mineralogy variations increases the regional and temporal variability of dust SSA compared to that of a compositionally homogeneous dust species, bringing the model SSA range closer to the observed one.

Our analyses support the need for more observations of iron oxides in soils and airborne dust, ideally providing information not only on the bulk iron oxides mass, but also on their speciation (e.g., in hematite and/or goethite) and size distribution. Improved soil mineralogy maps, such as those that will arise from high quality spaceborne hyperspectral measurements in  
795 the framework of the NASA EMIT project (Green et al., 2020) and field measurements of the emitted dust PSD and its composition (e.g., Panta et al., 2022; González-Flórez et al., 2022), will strongly contribute towards constraining the effects of dust mineralogy upon climate.

All in all, the mineralogy of atmospheric dust shows significant regional variations. Neglecting those variations in **modelling**  
modeling frameworks can affect not only our estimates of the regional variability of dust absorption of solar radiation, but also  
800 the total iron emission and the chemical interactions that lead to its solubilization in the atmosphere. The abundance of minerals such as quartz or feldspars within mixed-phase clouds, which is influenced by their size distribution, impacts ice formation (Chatziparaschos et al., 2023), which remains an important source of uncertainty in current model estimates of the climate forcing.

*Data availability.* The C1999-SMA and J2014-SMA used in this work will be publicly available at 0.0833°x0.0833° resolution upon  
805 manuscript acceptance. The multi-annual mean of the atmospheric mineral fractions in the C1999 and J2014 experiments will also be published at different pressure levels.

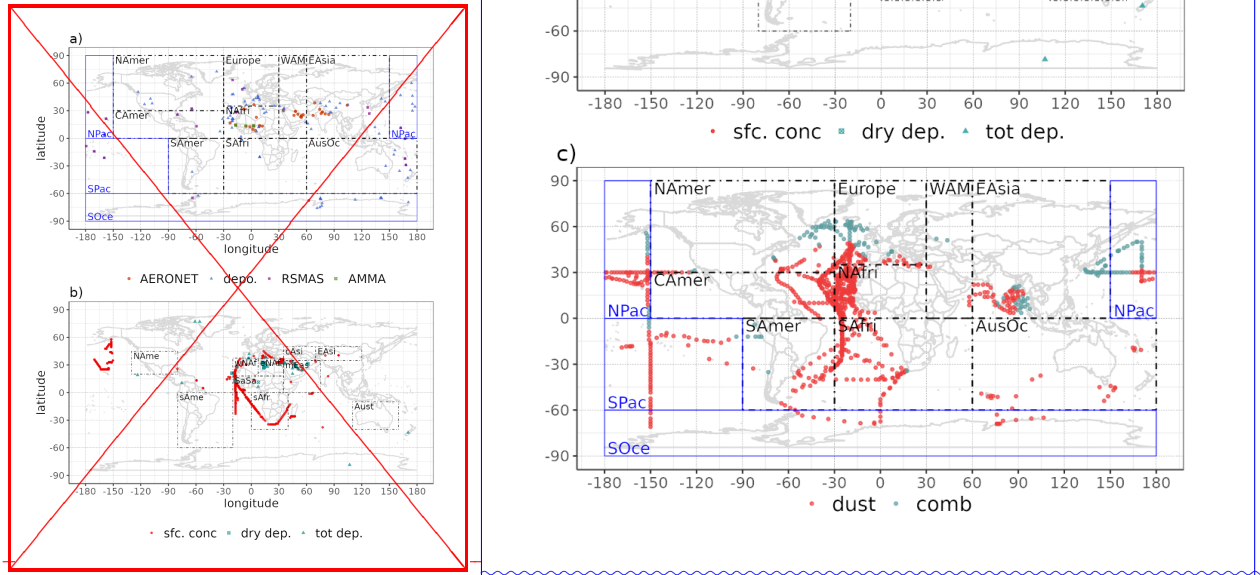


**Figure 2.** a) Location of the surface concentration (RSMAS, AMMA) and deposition (depo.) observations used for the dust evaluation, and domains defined to compute regional statistics (in boxes). The 35 AERONET sites resulting from the filtering for dust events described in section 4.3 are represented with red dots in the map. b) Location of the samples of mass mineral fractions in dust surface concentration (sfc. conc.), dry (dry dep.) and total deposition (tot. dep.) used in this study. Source regions, as defined by Kok et al. (2021), considered for the regional analyses are depicted with boxes. c) Location of the total iron concentration measurements from Myriokefalitakis et al. (2018). Red dots correspond to those influenced by dust aerosols and used for evaluation purposes in this study.



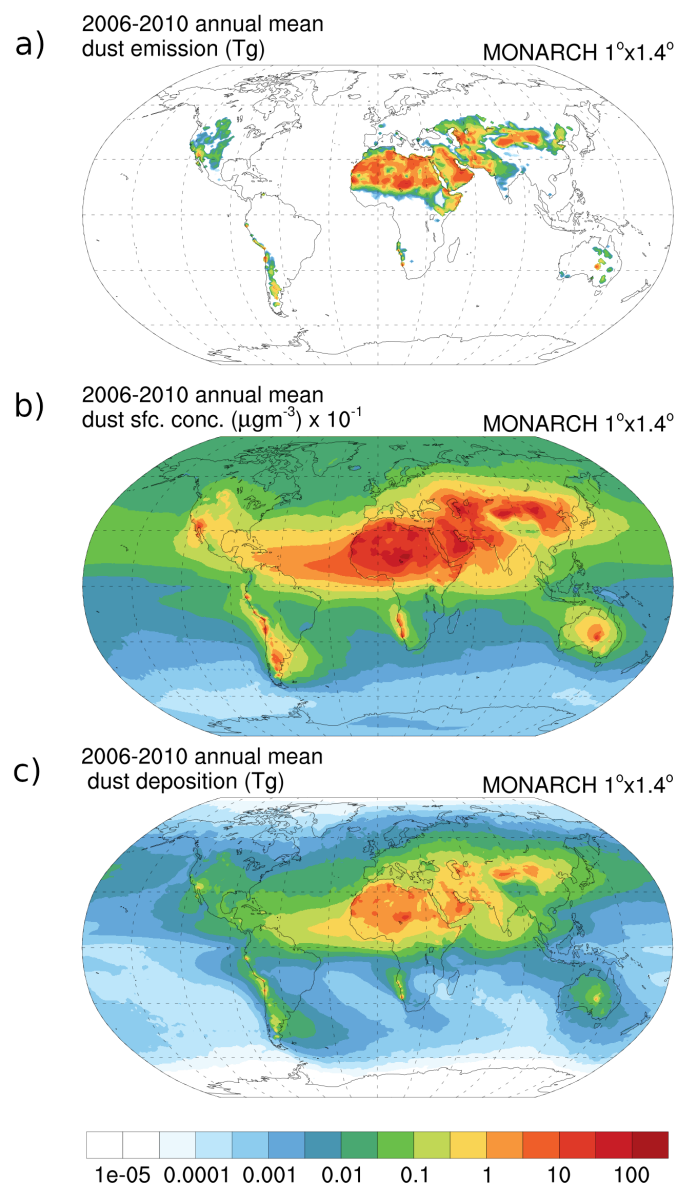


**Figure 3.** MONARCH ~~modelled~~modeled homogeneous (a) dust annual mean emission (Tg), (b) surface concentration ( $\mu\text{gm}^{-3}$ )  $\times 10^{-1}$ , and (c) total deposition (Tg), averaged over 2006-2010.

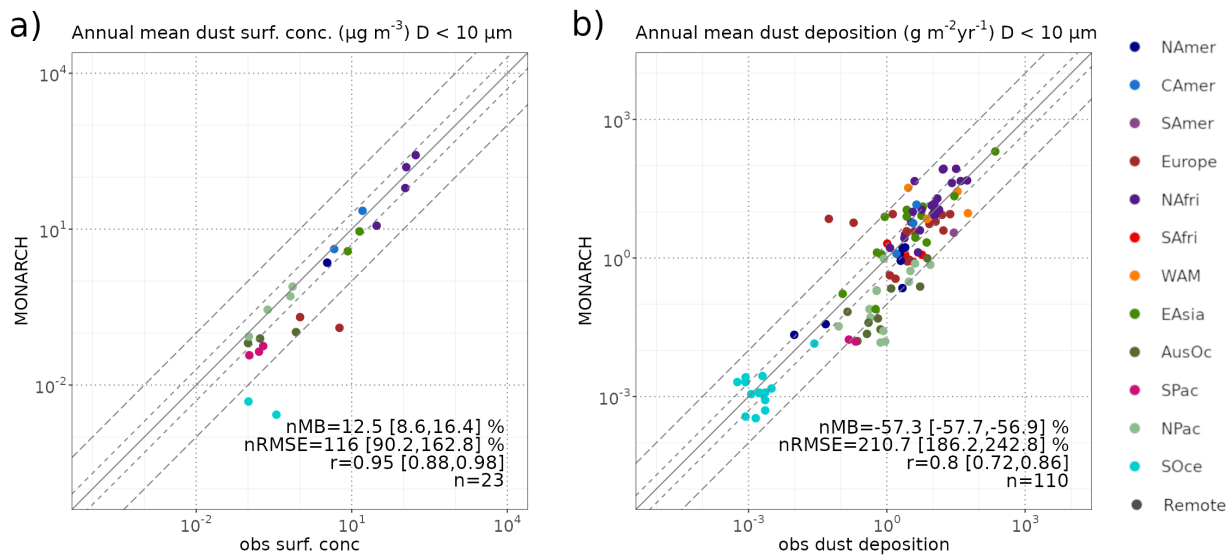


**Figure 4.** MONARCH ~~modelled~~ modeled annual mean (a) dust surface concentration ( $\mu\text{g m}^{-3}$ ) and (b) total deposition flux ( $\text{g m}^{-2} \text{y}^{-1}$ ) compared to observations from the RSMAS and INDAAF databases (left), and the compilation of Albani et al. (2014) (right). Where n is the number of measurements, nRMSE, the normalized Mean Root Square Error, nMB, the normalized Mean Bias, and r, the correlation, over all points. The ranges for the nMB, nRMSE and r correspond to the 95% confidence level (see ~~Section~~ section 1 of the Supplement for details). Regions are depicted in Figure 1a. Ashed lines represent differences of 2 times and one order of magnitude.

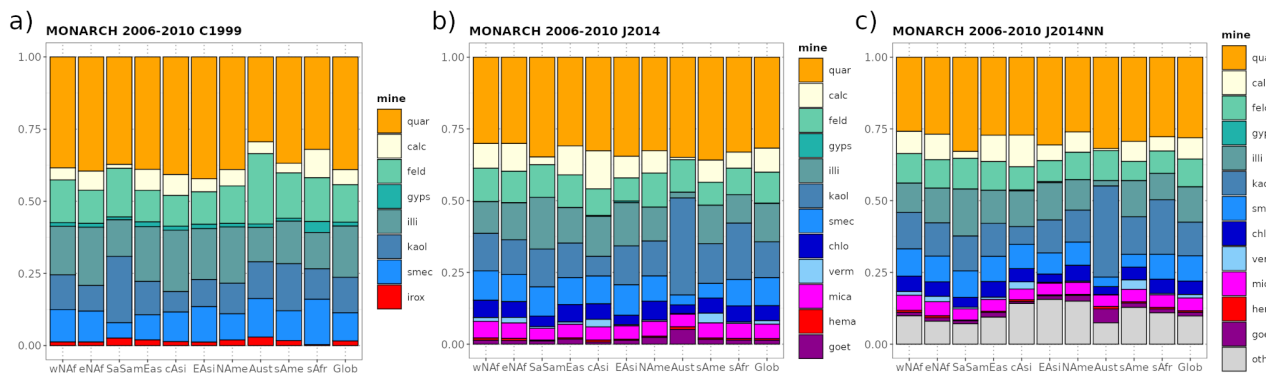


**Figure 5.** Mineral mass fractions at emission per region (as defined in Figure 2b) estimated by MONARCH C1999 (a), J2014 (b), and J2014NN (c), annual mean over 2006-2010. Where quar: quartz, calc: calcite, feld: feldspar, gyps: gypsum, illi: illite, kaol: kaolinite, smec: smectite, irox: iron oxides, chlo: chlorite, verm: vermiculite, mica: mica, hema: hematite, goet: goethite, and othr: other.

**Table 4.** Minerals mass fraction at emission, in the atmospheric burden and deposition at the global scale (%). Lifetime of the different minerals (days). Annual mean over 2006-2010. quar: quartz, calc: calcite, feld: feldspar, gyps: gypsum, illi: illite, kaol: kaolinite, smec: smectite, irox: iron oxides, chlo: chlorite, verm: vermiculite, mica: mica, hema: hematite, goet: goethite, and other: other.

<b>C1999</b>	<b>quar</b>	<b>calc</b>	<b>feld</b>	<b>gyps</b>	<b>illi</b>	<b>kaol</b>	<b>smec</b>	<b>chlo</b>	<b>verm</b>	<b>mica</b>	<b>hema</b>	<b>goet</b>	<b>phyl</b>	<b>irox</b>	<b>othr</b>
Emission (%w)	39.0	5.2	13.0	1.4	17.7	12.3	9.7	0.0	0.0	0.0	1.6	0.0	39.8	1.6	0.0
Burden (%w)	34.3	4.7	11.8	1.3	20.3	15.0	11.1	0.0	0.0	0.0	1.7	0.0	46.3	1.7	0.0
Dry deposition (%w)	40.6	5.4	13.5	1.3	16.9	11.3	9.3	0.0	0.0	0.0	1.6	0.0	37.6	1.6	0.0
Wet deposition (%w)	37.2	5.0	12.3	1.4	18.6	13.6	10.2	0.0	0.0	0.0	1.7	0.0	42.4	1.7	0.0
Total deposition (%w)	39.2	5.2	13.0	1.4	17.6	12.2	9.7	0.0	0.0	0.0	1.6	0.0	39.5	1.6	0.0
Lifetime (days)	2.7	2.7	2.8	3.0	3.5	3.7	3.5	0.0	0.0	0.0	3.2	0.0	3.6	3.2	0.0
<b>J2014</b>	<b>quar</b>	<b>calc</b>	<b>feld</b>	<b>gyps</b>	<b>illi</b>	<b>kaol</b>	<b>smec</b>	<b>chlo</b>	<b>verm</b>	<b>mica</b>	<b>hema</b>	<b>goet</b>	<b>phyl</b>	<b>irox</b>	<b>othr</b>
Emission (%w)	31.7	8.4	10.8	0.1	13.4	12.4	9.8	5.2	1.2	5.0	0.6	1.4	47.1	1.9	0.0
Burden (%w)	27.6	8.2	9.6	0.1	15.6	14.5	11.3	5.2	1.5	4.2	0.7	1.5	52.4	2.1	0.0
Dry deposition (%w)	32.8	8.5	11.4	0.1	12.5	11.8	9.3	5.2	1.2	5.3	0.5	1.4	45.3	1.9	0.0
Wet deposition (%w)	30.4	8.3	10.1	0.1	14.4	13.2	10.4	5.2	1.3	4.6	0.6	1.4	49.1	2.0	0.0
Total deposition (%w)	31.9	8.4	10.8	0.1	13.3	12.4	9.7	5.2	1.2	5.0	0.5	1.4	46.9	1.9	0.0
Lifetime (days)	2.7	3.0	2.7	2.6	3.6	3.6	3.6	3.0	3.7	2.6	3.6	3.2	3.4	3.4	0.0
<b>J2014NN</b>	<b>quar</b>	<b>calc</b>	<b>feld</b>	<b>gyps</b>	<b>illi</b>	<b>kaol</b>	<b>smec</b>	<b>chlo</b>	<b>verm</b>	<b>mica</b>	<b>hema</b>	<b>goet</b>	<b>phyl</b>	<b>irox</b>	<b>othr</b>
Emission (%w)	28.1	7.4	9.7	0.1	12.3	11.7	8.8	4.7	1.2	4.5	0.5	1.3	43.1	1.8	9.8
Burden (%w)	24.6	7.3	8.7	0.1	14.3	13.7	10.3	4.7	1.5	3.8	0.6	1.3	48.3	2.0	9.1
Dry deposition (%w)	29.1	7.5	10.2	0.1	11.5	11.2	8.4	4.7	1.1	4.8	0.5	1.2	41.6	1.8	9.7
Wet deposition (%w)	26.9	7.3	9.1	0.1	13.2	12.3	9.3	4.7	1.3	4.1	0.5	1.3	44.8	1.8	10.0
Total deposition (%w)	28.2	7.4	9.7	0.1	12.2	11.6	8.7	4.7	1.2	4.5	0.5	1.3	42.9	1.8	9.8
Lifetime (days)	2.7	3.0	2.7	2.6	3.6	3.6	3.6	3.1	3.7	2.6	3.6	3.3	3.4	3.4	2.8

This table only shows relative fractions, the corresponding totals are provided in Table S4 of the Supplement

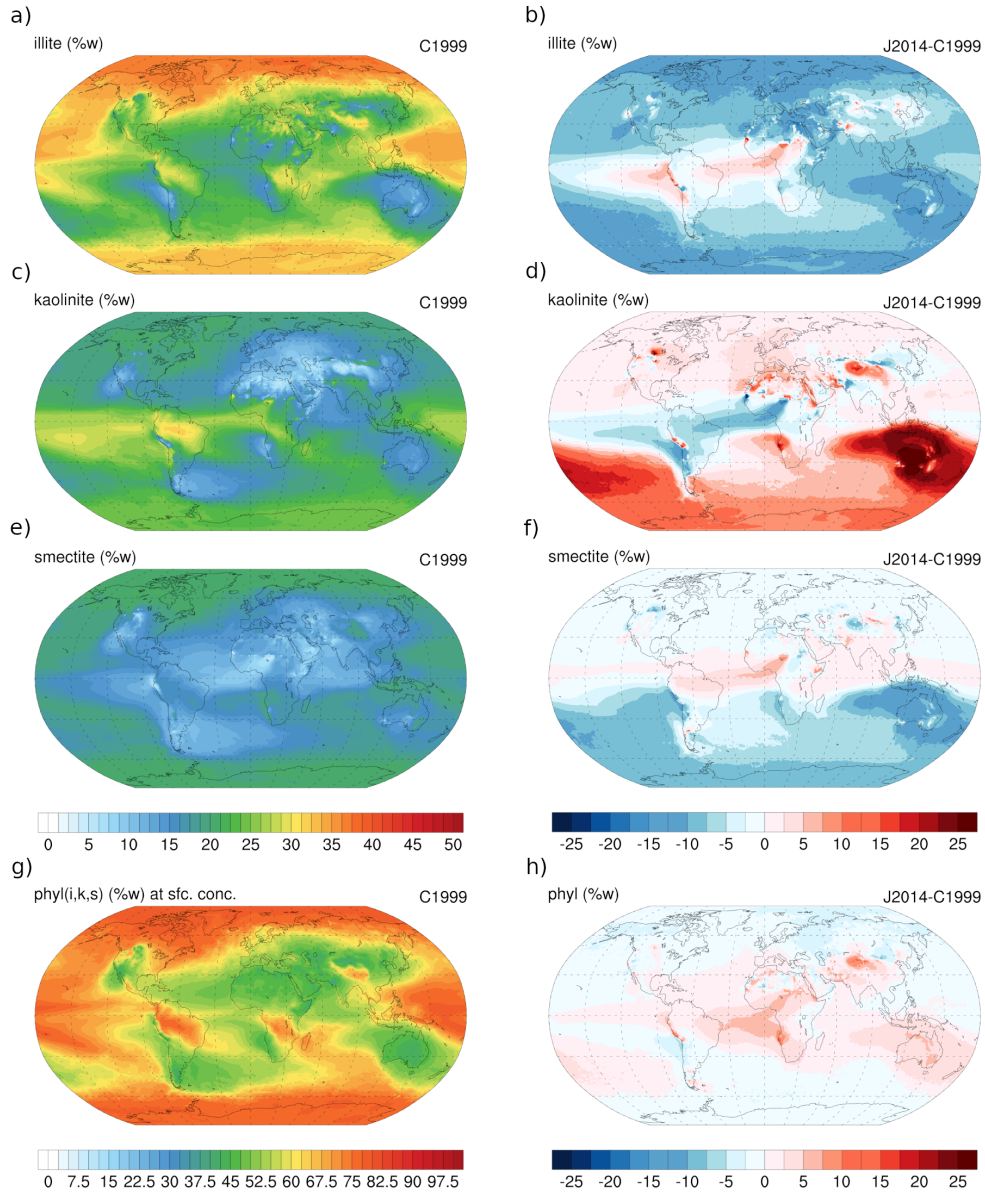


**Figure 6.** Annual mean (a) illite, (c) kaolinite, (e) smectite, and the (g) sum of all clay minerals mass fractions (%w) at surface concentration in C1999, and differences of annual mean (b) illite, (d) kaolinite, (f) smectite, and (h) all clay minerals mass fractions (%w) at surface concentration in J2014 with respect to C1999.

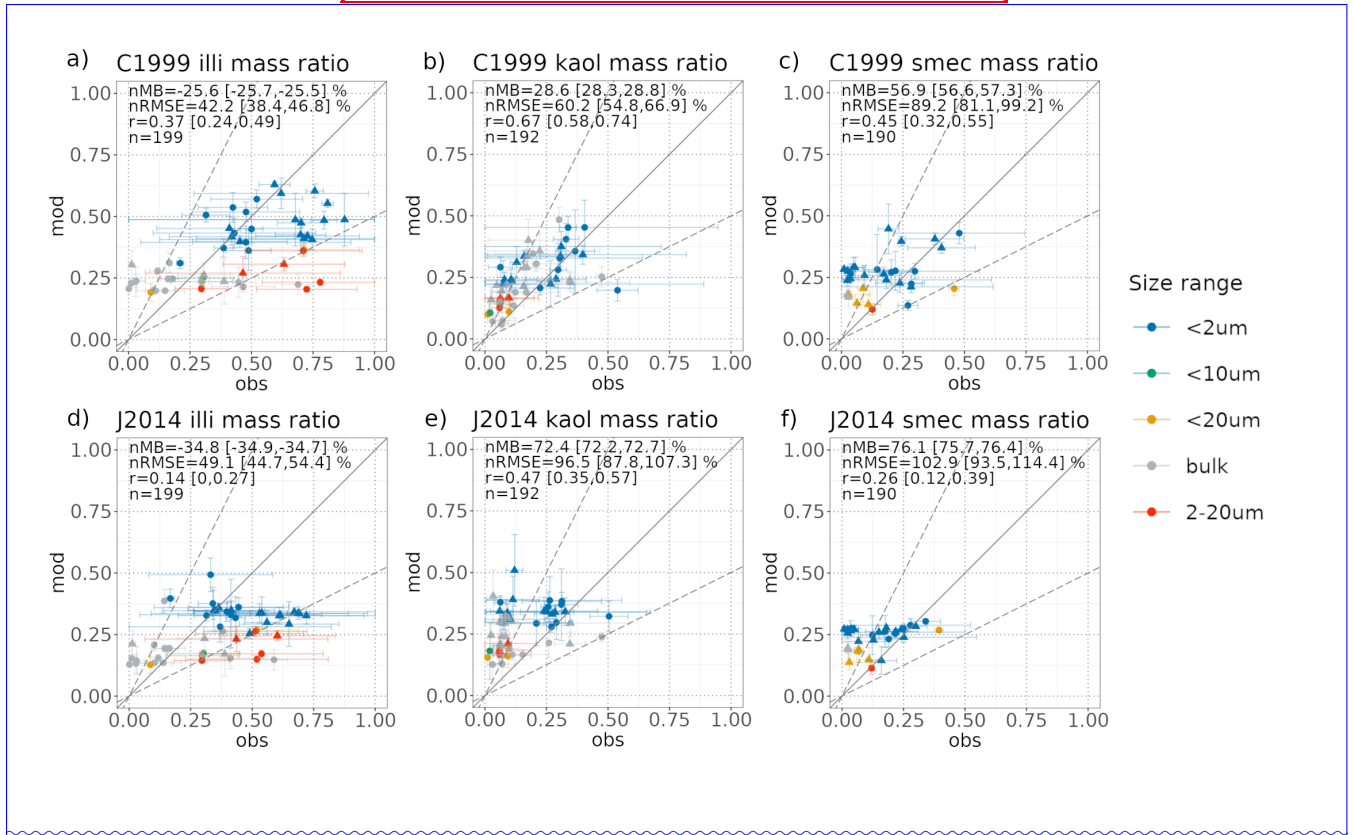
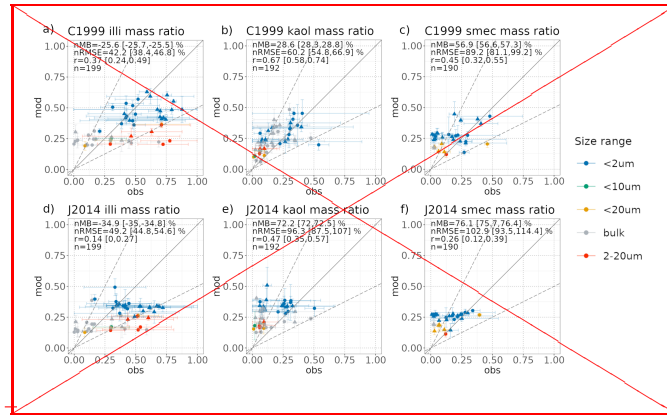


**Figure 7.** Comparison of the illite -illi-, kaolinite -kaol- and smectite -smec- ~~modelled-modeled~~ vs. observed mass fractions in the C1999 (panels a,b and c, respectively) and J2014 (panels d,e, and f, respectively) experiments. Colors identify size ranges, circles correspond to observation points that fall within source regions as depicted in Figure 2b and triangles to those outside. Statistics considering mean values are computed for all points within the ~~modelled-modeled~~ size ranges (up to 20  $\mu\text{m}$  of diameter). The ranges for the nMB, nRMSE and r correspond to the 95% confidence level (see ~~Section-section~~ 1 of the Supplement for details).

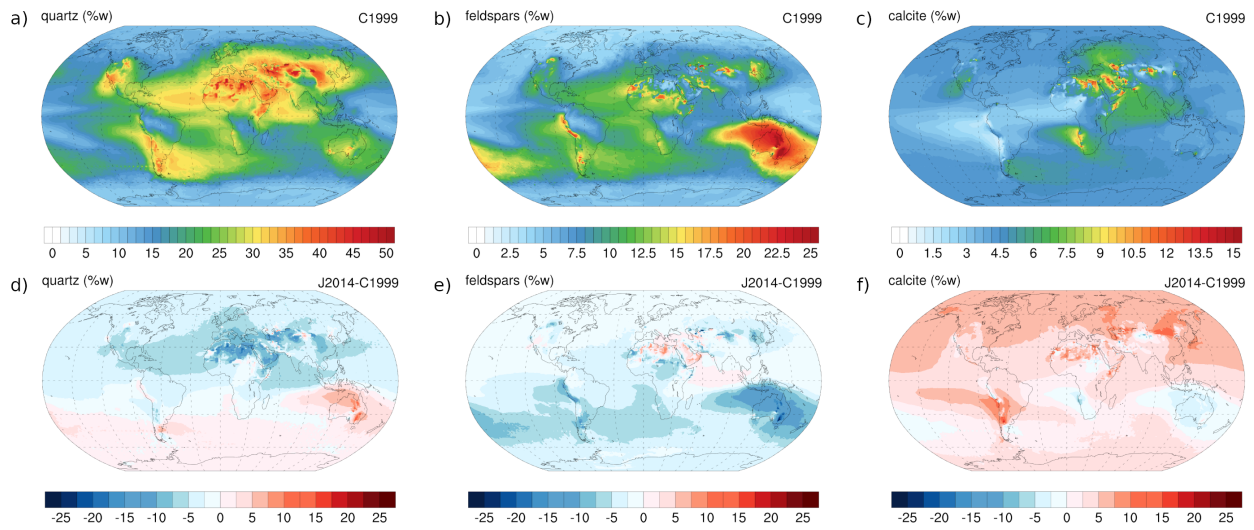


**Figure 8.** Annual mean (a) quartz, (b) feldspars, and (c) calcite mass fractions (%w) at surface concentration in C1999, and differences of annual mean (d) quartz, (e) feldspars, and (f) calcite mass fractions (%w) at surface concentration in J2014 with respect to C1999.

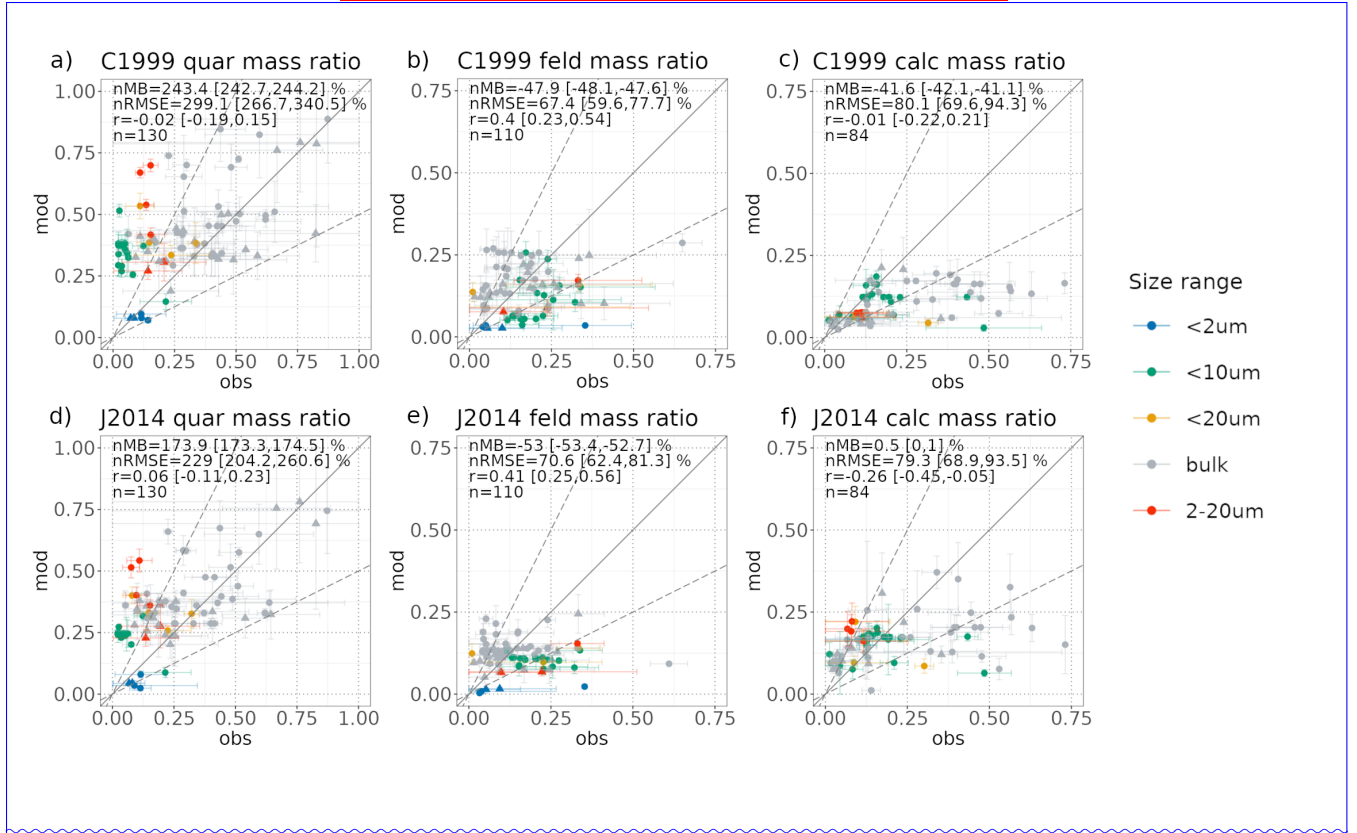
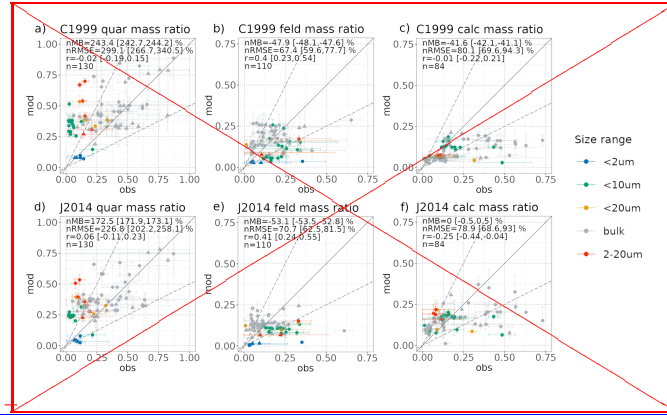


**Figure 9.** Comparison of the quartz -quar-, feldspar -feld- and calcite -calc- ~~modelled~~-modeled vs. observed mass fractions in the C1999 (panels a,b and c, respectively) and J2014 (panels d,e, and f, respectively) experiments. Colors identify size ranges, circles correspond to observation points that fall within source regions as depicted in Figure 2b and triangles to those outside. Statistics considering mean values are computed for all points within the ~~modelled~~-modeled size ranges (up to 20  $\mu\text{m}$  of diameter). The ranges for the nMB, nRMSE and r correspond to the 95% confidence level (see ~~Section~~-section 1 of the Supplement for details).



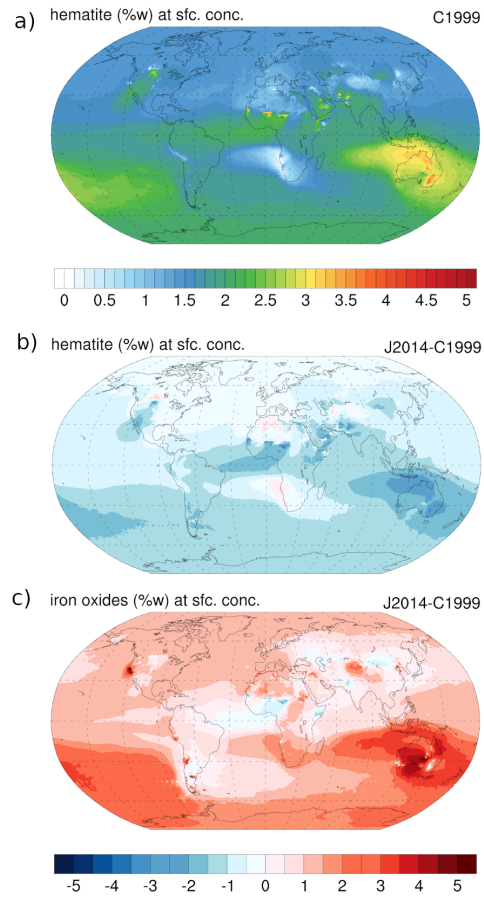


**Figure 10.** Annual mean hematite (iron oxides) mass fraction (%w) in surface concentration in C1999 (a), and differences compared to hematite in J2014 (b) and to iron oxides (hematite plus goethite) in J2014 (c).

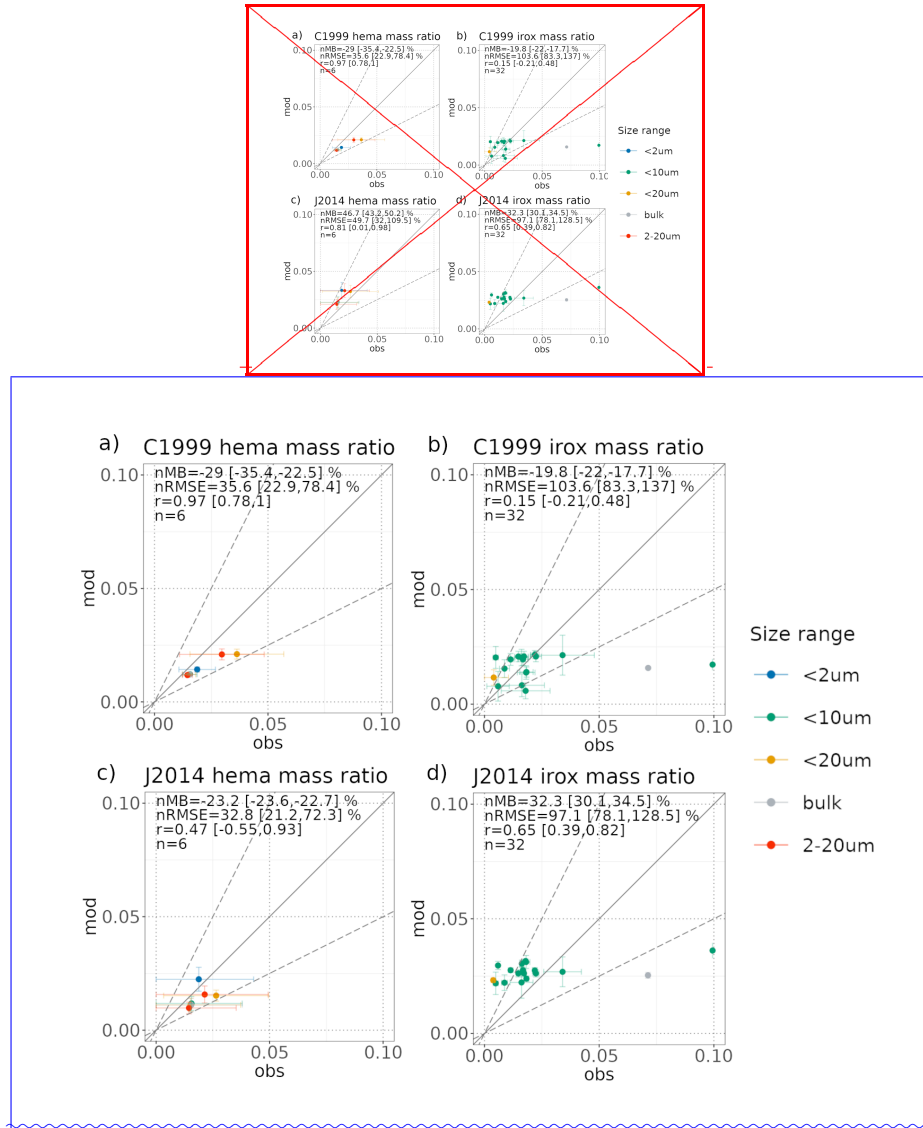


**Figure 11.** Comparison of the hematite -hema- and total iron oxides -irox- (from left to right) ~~modelled~~-modeled versus observed mass fractions in the C1999 (a and b, respectively) and J2014 (c and d, respectively) experiments. Colors identify size ranges, circles correspond to observation points that fall within source regions as depicted in Figure 2b and triangles to those outside. Statistics considering mean values are computed for all points within the ~~modelled~~-modeled size ranges (up to 20  $\mu\text{m}$  of diameter). The ranges for the nMB, nRMSE and r correspond to the 95% confidence level (see ~~Section~~-section 1 of the Supplement for details).

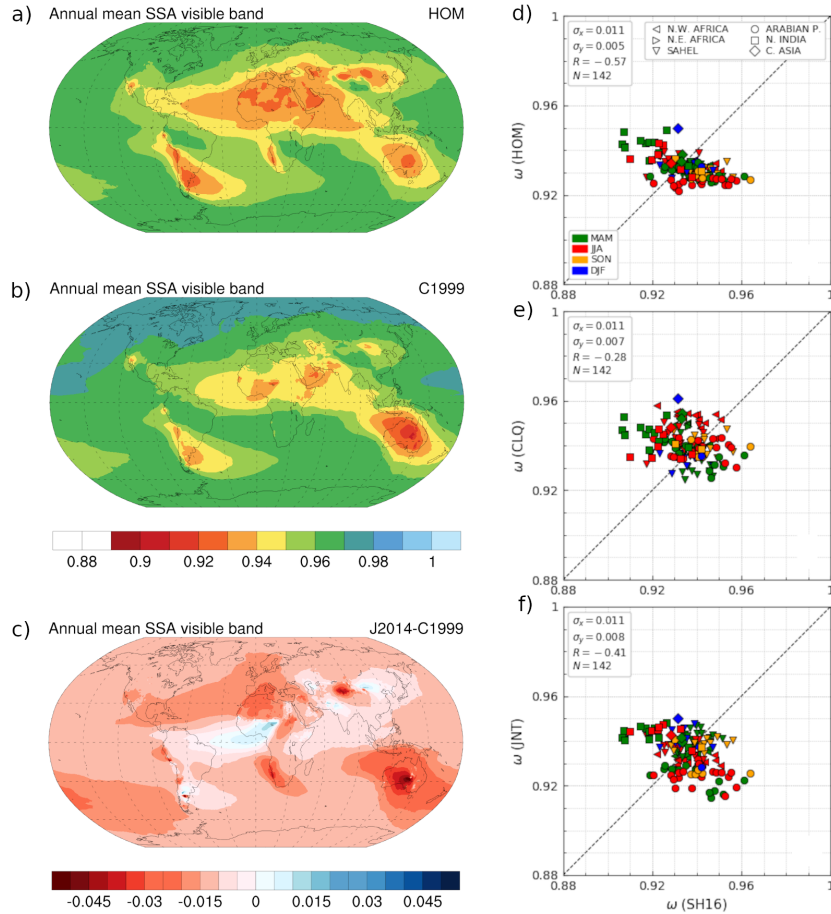


**Figure 12.** Annual mean Single Scattering Albedo (SSA), averaged in the ultra-violet (UV) and visible (VIS) band ( $0.3 - 0.77 \mu m$ ), considering dust as an optically homogeneous species (a), as the sum of three optically different species using C1999 modelled-modeled mineralogy (b), and differences between the latter and J2014 modelled-modeled mineralogy (c). Comparison of monthly mean UV-VIS SSA, calculated considering dust as a homogeneous species (d), and the mineralogy provided by C1999 (e) and J2014 (f), against dust-filtered SSA (averaged in the UV-VIS band) from AERONET version 3 level 2.0 Almucantar retrievals, at the selected AERONET stations and months, labeled by region and season.

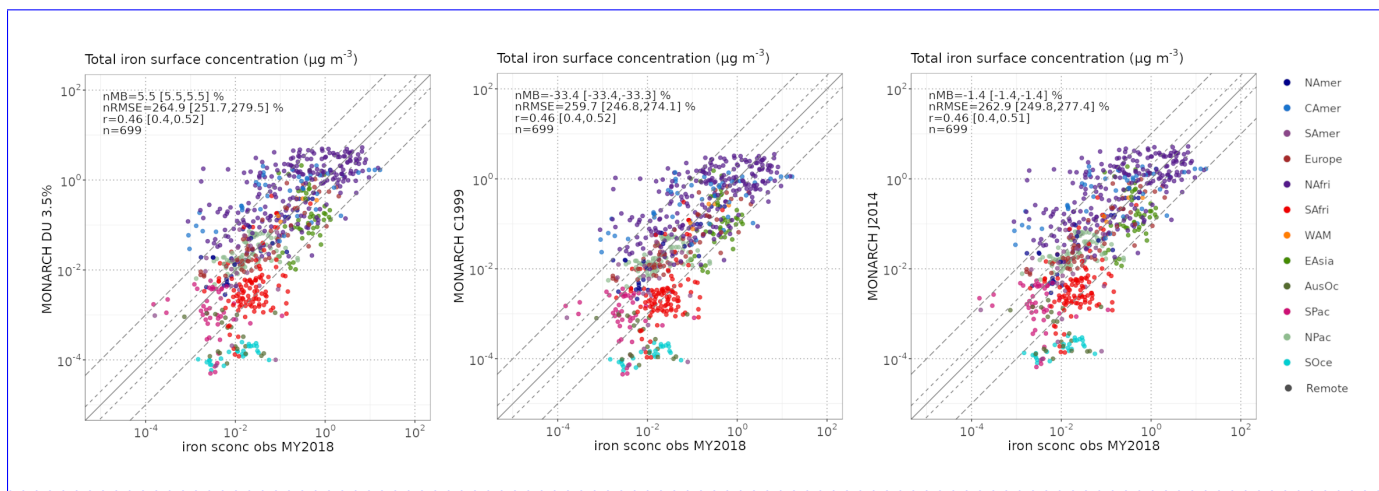


**Figure 13.** Diagnostic of the total iron surface concentration ( $\mu\text{g m}^{-3}$ ) associated to the MONARCH modeled (a) dust with an average 3.5w% of iron content, (b) C1999 and (c) J2014 dust mineralogy compared the observations compiled in Myriokefalitakis et al. (2018) identified as dust-dominated (see Figure 1c and section 4.4). Where n is the number of measurements, nRMSE, the normalized Mean Root Square Error, nMB, the normalized Mean Bias, and r, the correlation, over all points. The ranges for the nMB, nRMSE and r correspond to the 95% confidence level (see section 1 of the Supplement for details). Regions are depicted in Figure 1c. Ashed lines represent differences of 2 times and one order of magnitude.

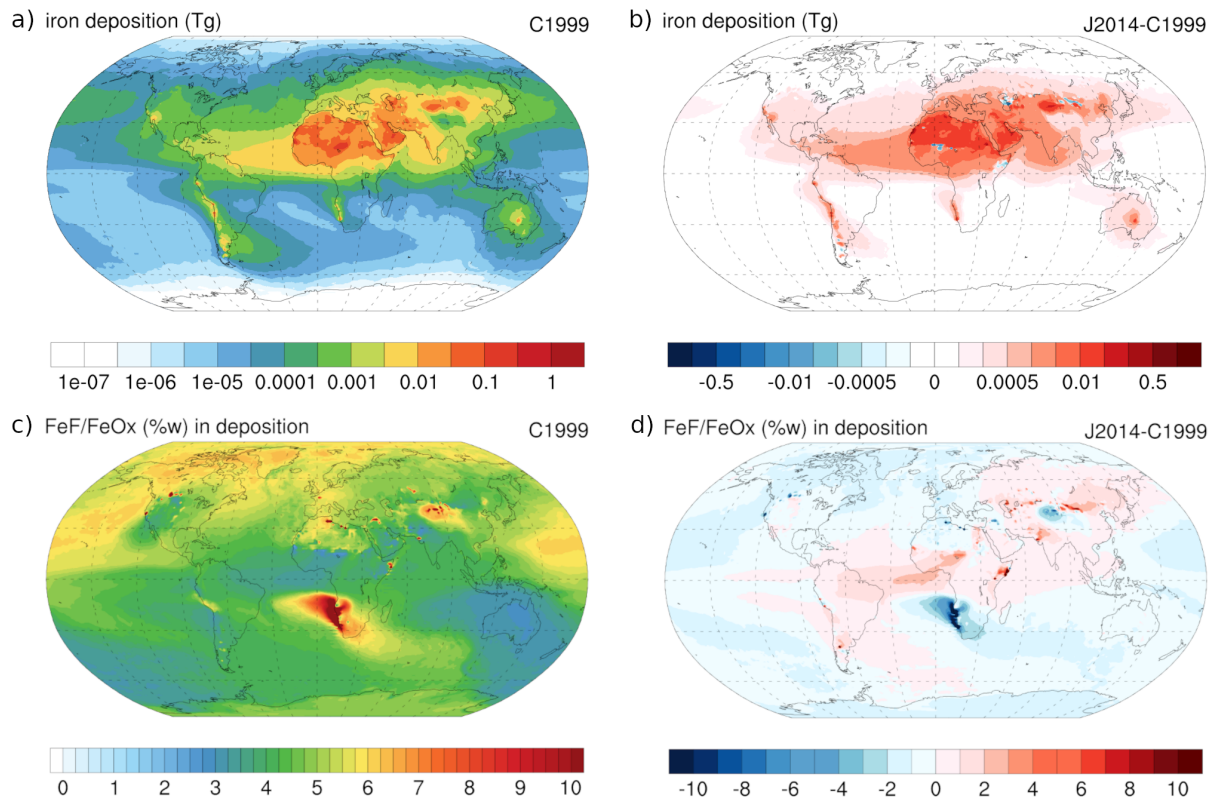


**Figure 14.** Total iron deposition and ratio of ferrihydrite and nano-iron oxides (FeF) over pure crystalline iron oxides (FeOx) according to C1999 (a and c, respectively), and differences compared to J2014 (b and d, respectively). The iron content of phyllosilicate minerals and feldspars is taken from Journet et al. (2014), and of hematite and goethite, from Journet et al. (2008). FeF is calculated as the sum of the fast and intermediate dissolution iron pools in Ito and Shi (2016), i.e., a 1.95 %w (0.65 %w and 1.3 %w, respectively) of the total iron.

## Appendix A: Review of currently available Soil Mineralogy Atlases

### A1 Main features of the Soil Mineralogy Atlases used in this study

The Soil Mineralogy Atlases used in this work come from Claquin et al. (1999), with revisions from Nickovic et al. (2012),  
810 C1999-SMA, and Journet et al. (2014), J2014-SMA. While C1999-SMA provides information on 8 minerals (illite, smectite, kaolinite, quartz, feldspars, calcite, gypsum, and hematite) for arid and semi-arid regions, J2014-SMA reports 4 additional minerals (chlorite, smectite, mica and goethite) with a global coverage (Table A1).

These maps give information on the mineralogy in two size classes of the soil: clay (up to 2  $\mu\text{m}$  in diameter) and silt (from  
815 2 to 63  $\mu\text{m}$  in diameter). The minerals are distributed in the same size ranges in both SMAs, except for feldspars, that are only present in silt sizes in C1999-SMA, but also in clay in J2014-SMA. Iron oxides, identified as hematite, are present both in the clay and silt sizes of the soil in C1999-SMA, while J2014-SMA distinguishes hematite, in the clay, from goethite, in both the clay and silt fractions.

Both SMAs describe the mineralogy of the soil after gathering mineral soil descriptions available in the literature and associating them to soil types from existing soil classification systems (i.e., from FAO). Once they attribute a mean mineralogy  
820 to a specific soil type, the geographical distribution of that soil type is used to create a map of soil composition either over arid and semi-arid regions (C1999-SMA), or else globally (J2014-SMA).

Claquin et al. (1999) use 239 soil descriptions to derive mean mineralogical composition for 25 soil types (FAO-UNESCO, 1974) provided by the FAO Digital Soil Map of the World (DSMW) (FAO-UNESCO, 1995). From the original analyses found in the literature, they are able to provide mineralogical information for approximately 80% of the soil types identified as arid  
825 or semi-arid. They complete the mean mineralogy for the missing soil types by applying empirical relationships, e.g., inferring the apportionment of calcite in the clay and silt soil sizes or the quartz and feldspars ratio from soil texture information, and associating the soil hematite content to information about soil redness.

Nickovic et al. (2012) extend the original dataset of Claquin et al. (1999), adding three new soil types (Yermosols, Haplic Yermosols and Xerosols), which also have a presence in arid and semi-arid regions, and attribute the same amount (%w) of  
830 hematite to the clay fraction as reported in Claquin et al. (1999) for the silt-sized faction.

The horizontal resolution of the FAO DSMW and thus of the C1999-SMA dataset is 0.083° ( $\sim 10$  km at mid-latitudes). Note that the increased resolution available in Nickovic et al. (2012) results from the remapping of the FAO data onto a higher resolution grid (0.0083°,  $\sim 1$  km at mid-latitudes) to be compatible with soil texture data at that higher resolution, so that the higher resolution spatial variations are rarely the result of abundant mineral measurements.

835 Journet et al. (2014) relate soil mineral composition to the soil unit attribute rather than the soil type used by C1999-SMA, also relying on the FAO soil classification system, but updating the information source to the Harmonized World Soil Database (HWSD) version 1.1 (FAO/IIASA/ISRIC/ISSCAS/JRC, 2009), a raster with a native spatial resolution of 0.0083° ( $\sim 1$  km at mid-latitudes). In this work, we have applied the HWSD version 1.2 (FAO/IIASA/ISRIC/ISSCAS/JRC, 2012) for convenience. However, there are no differences regarding the soil units mapping. Worldwide coverage is provided through the combination  
840 of the original FAO74 (FAO-UNESCO, 1974) and the updated FAO90 (FAO-UNESCO, 1997) systems, and uses 220 soil units,

**Table A1.** Main characteristics of the C1999-SMA and J2014-SMA Soil Mineralogy Atlases.

C1999-SMA		J2014-SMA	
Minerals considered			
Clay (D <2μm)	Silt (D 2-63 μ m)	Clay (D <2μm)	Silt (D 2-63 μ m)
quartz	quartz	quartz	quartz
calcite	calcite	calcite	calcite
	feldspars	feldspars	feldspars
	gypsum		gypsum
illite		illite	
kaolinite		kaolinite	
smectite		smectite	
		vermiculite	
		chlorite	chlorite
			mica
hematite <sup>(*)</sup> (iron ox- ides)	hematite (iron ox- ides)	hematite	
		goethite	goethite
Horizontal resolution			
0.083°		0.0083°	
Geographical coverage			
arid areas		global	
Number of soil records			
239		>700	
Underlying soil classes			
FAO74 as mapped in DSMW 25(28)* soil types		FAO74 and FAO90 as mapped in HWSD, 211 soil units	

<sup>(\*)</sup>Originally Claquin et al. (1999) report the mean mineralogy for 25 soil types, Nickovic et al. (2012) added 3 more types, while extending the same hematite fraction as in silt to the clay size category and referring to both as total iron oxides

although 9 of them correspond to classes that are not relevant for mineralogy ~~modelling~~-modeling (i.e., glaciers, water bodies, rock outcrops, urban or humanly disturbed areas, non information classes, etc.), leaving a total of 211 soil units to consider.

The mean mineralogy provided by Journet et al. (2014) relies on more than 700 soil descriptions, which allow them to sample 55% of the FAO soil units, and to extend and/or improve the geographical coverage of Claquin et al. (1999). To complete the

845 missing information they apply similar approaches as in Claquin et al. (1999), again relying on soil texture data, soil color for



iron oxides and in-lab analyses (e.g., for the apportionment of iron oxides in hematite and goethite). Information on chlorite, mica, quartz and feldspars in the silt sizes is assigned for many soil units as an average of the mass fractions of the major soil groups, or the full silt dataset. Journet et al. (2014) further extend the mineralogy of the clay fraction providing two alternative maps. In this work, we rely on CASE2, which assigns the mineralogy of the major soil group to those soil units with missing  
850 information.

The increased number of soil classes in Journet et al. (2014) as compared to Claquin et al. (1999) and Nickovic et al. (2012), results in comparable or lower sample sizes to the characterization of the mineralogy per soil unit. Consequently, the resulting mean mineralogy is not necessarily more robust despite the increased number of soil descriptions used. Moreover, the spatial distribution of some soil units differs between the DSMW and the HWSD, which affects the resulting mineralogy maps.  
855 Finally, the increased geographical variability, expected due to the application of a higher resolution soil classes map, is for some minerals buffered due to the extrapolations done by averaging the limited measurements of mineralogical composition over multiple soil units.

## A2 Changes included in the original Soil Mineralogy Atlases

Our method to project the soil composition into the emitted size distribution redistributes the minerals in the clay sizes towards  
860 coarser aerosol diameters, to account for the disturbed soil size distribution reported in the soil maps (see [Section 2.3.2](#)). To apply this method, we need the minerals to be identified in both the clay and silt sizes of the soil. Therefore we modify the C1999-SMA and J2014-SMA to account for feldspars and hematite in both soil size classes, which will produce a more realistic emitted size distribution of these minerals, but also for gypsum. Gypsum is usually associated with the coarser silt soil fraction; we add it also to the clay although its presence there is minimal. Given the low abundance of this mineral in the soil  
865 maps, we do not expect a significant impact on the other clay-sized mineral abundances.

In C1999-SMA we infer a fraction of feldspars in the clay sizes ( $feldspars_{c_i}$ ) for each soil type ( $i$ ) that considers the fraction in the silt ( $feldspars_{s_i}$ ) and scales it according to the distribution of quartz in clay ( $quartz_{c_i}$ ) and silt ( $quartz_{s_i}$ ) fractions (eq. A1). We apply the same approach to the J2014-SMA soil units that have inferred feldspars information in the silt, but not in the clay.

$$870 \quad feldspars_{c_i} = feldspars_{s_i} \cdot \frac{quartz_{c_i}}{quartz_{s_i}} \quad (A1)$$

Both in C1999-SMA and J2014-SMA, the clay fraction of gypsum ( $gypsum_{c_i}$ ) in each soil type ( $i$ ) is obtained by scaling the corresponding silt fraction ( $gypsum_{s_i}$ ) with the ratio of calcite in clay ( $calcite_{c_i}$ ) and silt ( $calcite_{s_i}$ ) fractions (eq. A2).

$$gypsum_{c_i} = gypsum_{s_i} \cdot \frac{calcite_{c_i}}{calcite_{s_i}} \quad (A2)$$

Hematite is added in the C1999-SMA to the clay fraction in the same proportion as it is present in the silt, following Nickovic  
875 et al. (2012). The added amount of feldspars and gypsum, in C1999-SMA and J2014-SMA, and of hematite in C1999-SMA is proportionally removed from the rest of minerals present in the clay fraction.

**Table A2.** Corrected clay-sized mineralogy associated to the Acrisols Haplic soil unit in J2014-SMA (%w).

SU	illi	smec	kaol	chlo	verm	feld	quar	calc	hema	goet
Acrisols Haplic	17.46	3.91	0	7.58	4.57	0	5.22	0.25	0.85	7.9

When generating the J2014-SMA map, we found small differences by combining the HWSDv1.2 FAO codes with the mean mineralogy table provided in Journet et al. (2014), and the actual maps published in their work. Some of the differences in the clay fraction arise from a typo in the article for the Acrisols haplic composition (Table A2), which influences mainly the mineralogy of soils over the Amazon region or central Africa. Also, in their analyses, the mass fractions of calcite and goethite in the silt sizes for Fluvisols, Calcisols haplic, Andosols, and Luvisols Orthic are derived from extensions of the original dataset. In this revision process, we decided to keep the original values reported in the Supplementary Materials of the article (Journet et al., 2014), which are derived from the compilation of soil descriptions.

The HWSDv1.2 raster provides high resolution information of the geographical distribution of the FAO90 and FAO74 soil units by code. Correspondence between those numerical codes and the actual soil units is provided in the HWSDv1.2 database. During the revision, we detected a discrepancy in the HWSDv1.2 database, in which the FAO74 codes for the Fluvisols units differ depending on the source of information (i.e., the HWSD\_DATA compared to the D\_SYMBOL74 data sheets). After correspondence with the database developers, we confirmed that the correct assignation for those soil units is: FAO74 code 147, Fluvisols Eutric (Je), code 148, Fluvisols Calcaric (Jc), and code 149, Fluvisols Dystric (Jd).

Figures ~~S3 to S8 in the Supplementary Materials~~ [S6 to S11 in the Supplement](#) show the distribution of mineral fractions in the clay and silt sizes for the C1999-SMA and J2014-SMA (normalized) after this revision process, considering the dominant soil types at a 0.5° x 0.5° resolution. The soil maps at 0.083° x 0.083° resolution are provided in netCDF files (see the Data availability section, for details).

*Author contributions.* MGA: conceptualization, formal analysis, investigation, methodology, software, validation, visualization, funding acquisition, resources, supervision, writing - original draft preparation. VO: conceptualization, formal analysis, investigation, methodology, validation, visualization, writing - review and editing. RLM: conceptualization, methodology, supervision, writing - review and editing. OJ, MD, MK, SB, EDT, JE: methodology, software, writing - review and editing. FM, GM: software, data curation. YB, JP: methodology, writing - review and editing. NMM, ROG, DRT: writing - review and editing. CPGP: conceptualization, formal analysis, methodology, funding acquisition, resources, supervision, project administration, writing - review and editing.

*Competing interests.* The authors declare that they have no conflict of interest.

*Acknowledgements.* We thank Dr. Akinori Ito and the anonymous reviewer who, with their comments, contributed to improve this manuscript quality.

This work was funded by the European Research Council under the Horizon 2020 research and innovation programme through the ERC  
905 Consolidator Grant FRAGMENT (grant agreement No. 773051), the AXA Research Fund through the AXA Chair on Sand and Dust Storms  
at BSC, the Spanish Ministerio de Economía y Competitividad through the NUTRIENT project (CGL2017-88911-R), the European Union's  
Horizon 2020 research and innovation programme under grant agreement No 821205 (FORCeS), and ESA through the DOMOS project  
(ESA AO/I-10546/20/I-NB). We ~~acknowledge the NASA~~ also acknowledge the support of the Department of Research and Universities of  
the Government of Catalonia to the Research Group Atmospheric Composition (Code: 2021 SGR 01550). We acknowledge the National  
910 Aeronautics and Space Administration (NASA) EMIT project, which is supported by the ~~National Aeronautics and Space Administration~~  
NASA Earth Venture Instrument program, under the Earth Science Division of the Science Mission Directorate. A portion of this research  
was carried out at the Jet Propulsion Laboratory, California Institute of Technology, under a contract with the National Aeronautics and Space  
Administration (80NM0018D0004).

RLM received support from the NASA Modeling, Analysis and Prediction Program (NNG14HH42I) along with the NASA EMIT  
915 project ~~funded by the Earth-Venture Instrument program.~~ VO was supported by the NASA Postdoctoral Program at the NASA Goddard  
Institute for Space Studies, administered by Oak Ridge Associated Universities under contract with NASA. JE and MK have received  
funding from the European Union's Horizon 2020 research and innovation programme under the Marie Skłodowska-Curie grant agree-  
ments H2020-MSCA-COFUND-2016-754433 and H2020-MSCA-IF-2017-789630, respectively. MK received further support through the  
Helmholtz Association's Initiative and Networking Fund (grant no. VH-NG-1533).

920 The authors gratefully acknowledge the AERONET and RSMAS PI(s) and their staff for establishing and maintaining the sites and  
data used in this investigation. PM10 measurements in Banizoumbou (Niger), Cinzana (Mali), M'Bour (Senegal) were performed in the  
framework of the French National Observatory Service INDAAF (International Network to study Deposition and Atmospheric composition  
in Africa; <https://indaaf.obs-mip.fr/>) piloted by the LISA and LAERO and supported by the INSU/CNRS, the IRD and the Observatoire Midi-  
Pyrénées and the Observatoire des Sciences de l'Univers EFLUVE. We also wish to thank the Harmonized World Soil Database developers  
925 from FAO, IIASA, ISRIC-World Soil Information, Institute of Soil Science, Chinese Academy of Sciences (ISSCAS), and the Joint Research  
Centre of the European Commission (JRC) for openly publishing their data and for answering our queries.

We thank all the members of the Computational Earth Sciences and Atmospheric Composition groups of the BSC, for their help in  
designing, creating and maintaining the infrastructure that makes possible the simulations and analyses presented here, in particular we would  
like to mention A. Bou, R. Garatachea, C. Meikle, C. Tena and M. Guevara for their valuable contribution to developments and discussions  
930 related to this work. We would like also to acknowledge E. Journet for her kind advice in the review process of the soil mineralogy map.

We acknowledge PRACE (eDUST, eFRAGMENT1 and eFRAGMENT2) and RES (AECT-2020-3-0020, AECT-2022-3-0013) for award-  
ing access to MareNostrum at the Barcelona Supercomputing Center and for providing technical support.

## References

- Albani, S., Mahowald, N. M., Perry, A., Scanza, R. A., Zender, C. S., Heavens, N., Maggi, V., Kok, J. F., and Otto-Bliesner, B.: Improved dust representation in the Community Atmosphere Model, *Journal of Advances in Modeling Earth Systems*, 6, 541–570, <https://doi.org/10.1002/2013MS000279>. Received, 2014.
- Arimoto, R., Duce, R. A., Ray, B. J., Ellis, W. G., Cullen, J. D., and Merrill, J. T.: Trace elements in the atmosphere over the North Atlantic, *Journal of Geophysical Research*, 100, 1199–1213, <https://doi.org/10.1029/94JD02618>, 1995.
- Atkinson, J. D., Murray, B. J., Woodhouse, M. T., Whale, T. F., Baustian, K. J., Carslaw, K. S., Dobbie, S., O’Sullivan, D., and Malkin, T. L.: The importance of feldspar for ice nucleation by mineral dust in mixed-phase clouds., *Nature*, 498, 355–8, <https://doi.org/10.1038/nclimate2153>, 2013.
- Badia, A. and Jorba, O.: Gas-phase evaluation of the online NMMB/BSC-CTM model over Europe for 2010 in the framework of the AQMEII-Phase2 project, *Atmospheric Environment*, 115, 657–669, <https://doi.org/10.1016/j.atmosenv.2014.05.055>, 2015.
- Badia, A., Jorba, O., Voulgarakis, A., Dabdub, D., Pérez García-Pando, C., Hilboll, A., Marfa, G., and Janjic, Z.: Description and evaluation of the Multiscale Online Nonhydrostatic Atmosphere Chemistry model (NMMB-MONARCH) version 1.0: Gas-phase chemistry at global scale, *Geoscientific Model Development*, 10, <https://doi.org/10.5194/gmd-10-609-2017>, 2017.
- Bergas-Massó, E., Gonçalves Ageitos, M., Myriokefalitakis, S., Miller, R. L., Noije, T. V., Le Sager, P., Montané, G., and García, P.: Pre-industrial, present and future atmospheric soluble iron deposition and the role of aerosol acidity and oxalate under CMIP6 emissions, *Earth’s Future*, 11, e2022EF003353, <https://doi.org/10.1029/2022EF003353>, 2023.
- Berrisford, P., Dee, D., Fielding, K., Fuentes, M., Kallberg, P., Kobayashi, S., and Uppala, S.: The ERA-Interim Archive, Tech. Rep. 1, <http://www.ecmwf.int/publications/library/do/references/list/782009>, 2009.
- Betts, A. K.: A new convective adjustment scheme. Part I: Observational and theoretical basis, *Quarterly Journal of the Royal Meteorological Society*, 112, 677–691, <https://doi.org/10.1002/qj.49711247307>, 1986.
- Betts, A. K. and Miller, M. J.: A new convective adjustment scheme. Part II: Single column tests using GATE wave, BOMEX, ATEX and arctic air-mass data sets, *Quarterly Journal of the Royal Meteorological Society*, 112, 693–709, <https://doi.org/10.1002/qj.49711247308>, 1986.
- Caquineau, S., Gaudichet, A., Gomes, L., Magonthier, M. C., and Chatenet, B.: Saharan dust: Clay ratio as a relevant tracer to assess the origin of soil-derived aerosols, *Geophysical Research Letters*, 25, 983–986, <https://doi.org/10.1029/98GL00569>, 1998.
- Caquineau, S., Gaudichet, A., Gomes, L., and Legrand, M.: Mineralogy of Saharan dust transported over northwestern tropical Atlantic Ocean in relation to source regions, *Journal of Geophysical Research*, 107, 4251, <https://doi.org/10.1029/2000JD000247>, 2002.
- Chatziparaschos, M., Daskalakis, N., Myriokefalitakis, S., Kalivitis, N., Nenes, A., Ageitos, M. G., Costa-Surós, M., García-pando, C. P., Zanolli, M., Vrekoussis, M., and Kanakidou, M.: Role of K-feldspar and quartz in global ice nucleation by mineral dust in mixed-phase clouds, *Atmospheric Chemistry and Physics*, p. 1785–1801, <https://doi.org/10.5194/acp-23-1785-2023>, 2023.
- Checa-Garcia, R., Balkanski, Y., Albani, S., Bergman, T., Carslaw, K., Cozic, A., Dearden, C., Marticorena, B., Michou, M., Van Noije, T., Nabat, P., O’Connor, F. M., Olivie, D., Prospero, J. M., Le Sager, P., Schulz, M., and Scott, C.: Evaluation of natural aerosols in CRESCENDO Earth system models (ESMs): Mineral dust, *Atmospheric Chemistry and Physics*, 21, 10295–10335, <https://doi.org/10.5194/acp-21-10295-2021>, 2021.
- Chester, R., Elderfield, H., Griffin, J. J., Johnson, L. R., and Padgham, R. C.: Eolian dust along the eastern margins of the Atlantic Ocean, *Marine Geology*, 13, 91–105, [https://doi.org/10.1016/0025-3227\(72\)90048-5](https://doi.org/10.1016/0025-3227(72)90048-5), 1972.

- 970 Chiapello, I., Bergametti, G., Chatenet, P., Bousquet, P., Dulac, F., and Santos Soares, E.: Origins of African dust transported over the northeastern tropical Atlantic, *Journal of Geophysical Research*, 102, 13 701–13 709, <https://doi.org/10.1029/97JD00259>, 1997.
- Claquin, T., Schulz, M., and Balkanski, Y. J.: Modeling the mineralogy of atmospheric dust sources, *Journal of Geophysical Research Atmospheres*, <https://doi.org/10.1029/1999JD900416>, 1999.
- Colette et al., A.: Copernicus Atmosphere Monitoring Service Regional Air Quality Forecasting System v1.0, in prep., in prep.
- 975 D’Almeida, G. A.: On the variability of desert aerosol radiative characteristics, *J. Geophys. Res.*, 92, <https://doi.org/10.1029/JD092iD03p03017>, 1987.
- Dawson, M. L., Guzman, C., Curtis, J. H., Acosta, M., Zhu, S., Dabdub, D., Conley, A., West, M., Riemer, N., and Jorba, O.: Chemistry Across Multiple Phases (CAMP) version 1.0: An integrated multi-phase chemistry model, pp. 3663–3689, <https://doi.org/10.5194/gmd-2021-370>, 2021.
- 980 Dee, D. P., Uppala, S. M., Simmons, A. J., Berrisford, P., Poli, P., Kobayashi, S., Andrae, U., Balmaseda, M. A., Balsamo, G., Bauer, P., Bechtold, P., Beljaars, A. C. M., van de Berg, L., Bidlot, J., Bormann, N., Delsol, C., Dragani, R., Fuentes, M., Geer, A. J., Haimberger, L., Healy, S. B., Hersbach, H., Hólm, E. V., Isaksen, I., Kallberg, P., Köhler, M., Matricardi, M., McNally, A. P., Monge-Sanz, B. M., Morcrette, J. J., Park, B. K., Peubey, C., de Rosnay, P., Tavolato, C., Thépaut, J. N., and Vitart, F.: The ERA-Interim reanalysis: Configuration and performance of the data assimilation system, *Quarterly Journal of the Royal Meteorological Society*, 137, 553–597, <https://doi.org/10.1002/qj.828>, 2011.
- 985 Di Biagio, C., Boucher, H., Caqueneau, S., Chevaillier, S., Cuesta, J., and Formenti, P.: Variability of the infrared complex refractive index of African mineral dust: experimental estimation and implications for radiative transfer and satellite remote sensing, *Atmospheric Chemistry and Physics*, 14, 11 093–11 116, <https://doi.org/10.5194/acp-14-11093-2014>, 2014.
- Di Biagio, C., Formenti, P., Balkanski, Y., Caponi, L., Cazaunau, M., Pangui, E., Journet, E., Nowak, S., Caqueneau, S., Andreae O, M., Kandler, K., Saeed, T., Piketh, S., Seibert, D., Williams, E., and Doussin, J. F. C.: Global scale variability of the mineral dust long-wave refractive index: A new dataset of in situ measurements for climate modeling and remote sensing, *Atmospheric Chemistry and Physics*, 17, 1901–1929, <https://doi.org/10.5194/acp-17-1901-2017>, 2017.
- 990 Di Biagio, C., Formenti, P., Balkanski, Y., Caponi, L., Cazaunau, M., Pangui, E., Journet, E., Nowak, S., Andreae, M. O., Kandler, K., Saeed, T., Piketh, S., Seibert, D., Williams, E., Doussin, J.-F. F., Biagio, C. D., Formenti, P., Balkanski, Y., Caponi, L., Cazaunau, M., Pangui, E., Journet, E., Nowak, S., Andreae, M. O., Kandler, K., Saeed, T., Piketh, S., Seibert, D., Williams, E., Doussin, J.-F. F., Di Biagio, C., Formenti, P., Balkanski, Y., Caponi, L., Cazaunau, M., Pangui, E., Journet, E., Nowak, S., Andreae, M. O., Kandler, K., Saeed, T., Piketh, S., Seibert, D., Williams, E., and Doussin, J.-F. F.: Complex refractive indices and single-scattering albedo of global dust aerosols in the shortwave spectrum and relationship to size and iron content, *Atmospheric Chemistry and Physics*, 19, 15 503–15 531, <https://doi.org/10.5194/acp-19-15503-2019>, 2019.
- 995 Di Biagio, C., Formenti, P., Balkanski, Y., Caponi, L., Cazaunau, M., Pangui, E., Journet, E., Nowak, S., Andreae, M. O., Kandler, K., Saeed, T., Piketh, S., Seibert, D., Williams, E., Doussin, J.-F. F., Di Biagio, C., Formenti, P., Balkanski, Y., Caponi, L., Cazaunau, M., Pangui, E., Journet, E., Nowak, S., Andreae, M. O., Kandler, K., Saeed, T., Piketh, S., Seibert, D., Williams, E., Doussin, J.-F. F.: Complex refractive indices and single-scattering albedo of global dust aerosols in the shortwave spectrum and relationship to size and iron content, *Atmospheric Chemistry and Physics*, 19, 15 503–15 531, <https://doi.org/10.5194/acp-19-15503-2019>, 2019.
- 1000 Di Tomaso, E., Schutgens, N. A., Jorba, O., and García-Pando, C. P.: Assimilation of MODIS Dark Target and Deep Blue observations in the dust aerosol component of NMMB-MONARCH version 1.0, *Geoscientific Model Development*, 10, 1107–1129, <https://doi.org/10.5194/gmd-10-1107-2017>, 2017.
- Di Tomaso, E., Escribano, J., Basart, S., Ginoux, P., Macchia, F., Barnaba, F., Benincasa, F., Bretonnière, P.-a., Buñuel, A., Castrillo, M., Cuevas, E., Formenti, P., Gonçalves, M., Jorba, O., Klose, M., Mona, L., Montané, G., Mytilinaios, M., Obiso, V., and Olid, M.: The MONARCH high-resolution reanalysis of desert dust aerosol over Northern Africa, the Middle East and Europe (2007-2016), *Earth System Science Data*, pp. 2785–2816, <https://doi.org/10.5194/essd-14-2785-2022>, 2022.
- 1005

- Dubovik, O., Holben, B., Eck, T. F., Smirnov, A., Kaufman, Y. J., King, M. D., Tanré, D., and Slutsker, I.: Variability of Absorption and Optical Properties of Key Aerosol Types Observed in Worldwide Locations, *Journal of the Atmospheric Sciences*, 59, 590–608, [https://doi.org/10.1175/1520-0469\(2002\)059<0590:VOAOP>2.0.CO;2](https://doi.org/10.1175/1520-0469(2002)059<0590:VOAOP>2.0.CO;2), 2002.
- 1010 Ek, M. B., Mitchell, K. E., Lin, Y., Rogers, E., Grunmann, P., Koren, V., Gayno, G., and Tarpley, J. D.: Implementation of Noah land surface model advances in the National Centers for Environmental Prediction operational mesoscale Eta model, *Journal of Geophysical Research: Atmospheres*, 108, 8851, <https://doi.org/10.1029/2002JD003296>, 2003.
- Escribano, J., Di Tomaso, E., Jorba, O., Klose, M., Gonçalves Ageitos, M., Macchia, F., Amiridis, V., Baars, H., Marinou, E., Proestakis, E., Urbanneck, C., Althausen, D., Bühl, J., Mamouri, R. E., and Pérez García-Pando, C.: Assimilating spaceborne lidar dust extinction can improve dust forecasts, *Atmospheric Chemistry and Physics*, 22, 535–560, <https://doi.org/10.5194/acp-22-535-2022>, 2022.
- 1015 FAO-UNESCO: Soil Map of the World- Volume I Legend, Food and Agriculture Organization - United Nations Educational Scientific and Cultural Organization, Paris, <http://www.fao.org/3/as360e/as360e.pdf>, 1974.
- FAO-UNESCO: Food and Agriculture Organization - United Nations Educational Scientific and Cultural Organization. Digital Soil Map of the World and Derived Soil Properties, Food and Agriculture Organization - United Nations Educational Scientific and Cultural Organization, Rome, 1995.
- 1020 FAO-UNESCO: Soil Map of the World, Revised Legend with corrections and updates. World Soil Resources Report 60. FAO, 1988. Reprinted with updates as Technical Paper 20, ISRIC, 1997, Food and Agriculture Organization - United Nations Educational Scientific and Cultural Organization, FAO, Rome, ISRIC, Wageningen, [http://www.fao.org/fileadmin/user\\_upload/soils/docs/isricu\\_i9264\\_001.pdf](http://www.fao.org/fileadmin/user_upload/soils/docs/isricu_i9264_001.pdf), 1997.
- FAO/IIASA/ISRIC/ISSCAS/JRC: Harmonized World Soil Database (version 1.1), Food and Agriculture Organization, FAO, Rome, Italy and IIASA, Laxenburg, Austria, 2009.
- 1025 FAO/IIASA/ISRIC/ISSCAS/JRC: Harmonized World Soil Database (version 1.2), Food and Agriculture Organization, FAO, Rome, Italy and IIASA, Laxenburg, Austria, 2012.
- Ferrier, B. S., Jin, Y., Lin, Y., Black, T., Rogers, E., and DiMego, G.: Implementation of a new grid-scale cloud and precipitation scheme in the NCEP Eta Model, in: *Proceedings of the 15th Conference on Numerical Weather Prediction*, pp. 280–283, American Meteorological Society, San Antonio (Texas), 2002.
- 1030 Formenti, P., Rajot, J. L., Desboeufs, K., Caquineau, S., Chevaillier, S., Nava, S., Gaudichet, A., Journet, E., Triquet, S., Alfaro, S., Chiari, M., Haywood, J., Coe, H., and Highwood, E.: Regional variability of the composition of mineral dust from western Africa: Results from the AMMA SOP0/DABEX and DODO field campaigns, *Journal of Geophysical Research Atmospheres*, 113, 1–12, <https://doi.org/10.1029/2008JD009903>, 2008.
- 1035 Formenti, P., Schütz, L., Balkanski, Y., Desboeufs, K., Ebert, M., Kandler, K., Petzold, A., Scheuven, D., Weinbruch, S., and Zhang, D.: Recent progress in understanding physical and chemical properties of African and Asian mineral dust, *Atmospheric Chemistry and Physics*, 11, 8231–8256, <https://doi.org/10.5194/acp-11-8231-2011>, 2011.
- Formenti, P., Caquineau, S., Desboeufs, K., Klaver, A., Chevaillier, S., Journet, E., and Rajot, J. L.: Mapping the physico-chemical properties of mineral dust in western Africa: mineralogical composition, *Atmospheric Chemistry and Physics*, 14, 10663–10686, <https://doi.org/10.5194/acp-14-10663-2014>, 2014.
- 1040 Giles, D. M., Sinyuk, A., Sorokin, M. G., Schafer, J. S., Smirnov, A., Slutsker, I., Eck, T. F., Holben, B. N., Lewis, J. R., Campbell, J. R., Welton, E. J., Korkin, S. V., and Lyapustin, A. I.: Advancements in the Aerosol Robotic Network (AERONET) Version 3 database-automated near-real-time quality control algorithm with improved cloud screening for Sun photometer aerosol optical depth (AOD) measurements, *Atmospheric Measurement Techniques*, 12, 169–209, <https://doi.org/10.5194/amt-12-169-2019>, 2019.

- 1045 Ginoux, P., Chin, M., Tegen, I., Prospero, J. M., Holben, B., Dubovik, O., and Lin, S.-J.: Sources and distributions of dust aerosols simulated with the GOCART model, *Journal of Geophysical Research*, 106, 20 255, <https://doi.org/10.1029/2000JD000053>, 2001.
- Ginoux, P., Prospero, J. M., Gill, T. E., Hsu, N. C., and Zhao, M.: Global scale attribution of anthropogenic and natural dust sources and their emission rates based on MODIS Deep Blue aerosol products, *Rev. Geophys*, 50, 3005, <https://doi.org/10.1029/2012RG000388>, 2012.
- Go, S., Lyapustin, A., Schuster, G. L., Choi, M., Ginoux, P., Chin, M., Kalashnikova, O., Dubovik, O., Kim, J., Da Silva, A., Holben, B., and  
1050 Reid, J. S.: Inferring iron-oxide species content in atmospheric mineral dust from DSCOVR EPIC observations, *Atmospheric Chemistry and Physics*, 22, 1395–1423, <https://doi.org/10.5194/acp-22-1395-2022>, 2022.
- Gomes, L. and Gillette, D. A.: A comparison of characteristics of aerosol from dust storms in Central Asia with soil-derived dust from other regions, *Atmospheric Environment*, 27, 2539–2544, [https://doi.org/10.1016/0960-1686\(93\)90027-V](https://doi.org/10.1016/0960-1686(93)90027-V), 1993.
- González-Flórez, C., Klose, M., Alastuey, A., Dupont, S., Escribano, J., Etyemezian, V., Gonzalez-romero, A., Huang, Y., Kandler, K., and  
1055 Nikolich, G.: Insights into the size-resolved dust emission from field measurements in the Moroccan Sahara, *Atmospheric Chemistry and Physics Discussions* [preprint], pp. 1–65, <https://doi.org/10.5194/acp-2022-758>, 2022.
- Goodman, A. L., Underwood, G. M., and Grassian, V. H.: A laboratory study of the heterogeneous reaction of nitric acid on calcium carbonate particles, *Journal of Geophysical Research Atmospheres*, 105, 29 053–29 064, <https://doi.org/10.1029/2000JD900396>, 2000.
- Green, R. O., Mahowald, N., Ung, C., Thompson, D. R., Bator, L., Bennet, M., Bernas, M., Blackway, N., Bradley, C., Cha, J., Clark,  
1060 P., Clark, R., Cloud, D., Diaz, E., Ben Dor, E., Duren, R., Eastwood, M., Ehlmann, B. L., Fuentes, L., Ginoux, P., Gross, J., He, Y., Kalashnikova, O., Kert, W., Keymeulen, D., Klimesh, M., Ku, D., Kwong-Fu, H., Liggett, E., Li, L., Lundeen, S., Makowski, M. D., Mazer, A., Miller, R., Mouroulis, P., Oaida, B., Okin, G. S., Ortega, A., Oyake, A., Nguyen, H., Pace, T., Painter, T. H., Pempejian, J., Garcia-Pando, C. P., Pham, T., Phillips, B., Pollock, R., Purcell, R., Realmuto, V., Schoolcraft, J., Sen, A., Shin, S., Shaw, L., Soriano, M., Swayze, G., Thingvold, E., Vaid, A., and Zan, J.: The Earth Surface Mineral Dust Source Investigation: An Earth Science Imaging  
1065 Spectroscopy Mission, in: 2020 IEEE Aerospace Conference, pp. 1–15, <https://doi.org/10.1109/AERO47225.2020.9172731>, 2020.
- Griffin, J. J., Windom, H., and Goldberg, E. D.: The distribution of clay minerals in the World Ocean, *Deep-Sea Research and Oceanographic Abstracts*, 15, 433–459, [https://doi.org/10.1016/0011-7471\(68\)90051-X](https://doi.org/10.1016/0011-7471(68)90051-X), 1968.
- Guerschman, J. P., Scarth, P. F., McVicar, T. R., Renzullo, L. J., Malthus, T. J., Stewart, J. B., Rickards, J. E., and Trevithick, R.: Assessing the effects of site heterogeneity and soil properties when unmixing photosynthetic vegetation, non-photosynthetic vegetation and bare soil  
1070 fractions from Landsat and MODIS data, *Remote Sensing of Environment*, 161, 12–26, <https://doi.org/10.1016/j.rse.2015.01.021>, 2015.
- Guzmán-Ruiz, C., Acosta, M., Dawson, M., Jorba, O., Pérez García-Pando, C., and Serradell, K.: Accelerating Chemistry Modules in Atmospheric Models using GPUs, in: NVIDIA’s GPU Technology Conference (GTC), GTC, San Jose, CA, USA, <http://hdl.handle.net/2117/331028>, 2020.
- Hamilton, D. S., Scanza, R. A., Feng, Y., Guinness, J., Kok, J. F., Li, L., Liu, X., Rathod, S. D., Wan, J. S., Wu, M., and Mahowald, N. M.:  
1075 Improved methodologies for Earth system modelling of atmospheric soluble iron and observation comparisons using the Mechanism of Intermediate complexity for Modelling Iron (MIMI v1.0), *Geosci. Model Dev*, 12, 3835–3862, <https://doi.org/10.5194/gmd-12-3835-2019>, 2019.
- Harrison, A. D., Lever, K., Sanchez-Marroquin, A., Holden, M. A., Whale, T. F., Tarn, M. D., Mcquaid, J. B., and Murray, B. J.: The ice-nucleating ability of quartz immersed in water and its atmospheric importance compared to K-feldspar, *Atmos. Chem. Phys*, 19,  
1080 11 343–11 361, <https://doi.org/10.5194/acp-19-11343-2019>, 2019.
- Haustein, K., Pérez, C., Baldasano, J. M., Jorba, O., Basart, S., Miller, R. L., Janjic, Z., Black, T., Nickovic, S., Todd, M. C., Washington, R., Müller, D., Tesche, M., Weinzierl, B., Esselborn, M., and Schladitz, A.: Atmospheric dust modeling from meso to global scales



- with the online NMMB/BSC-Dust model - Part 2: Experimental campaigns in Northern Africa, *Atmospheric Chemistry and Physics*, 12, 2933–2958, <https://doi.org/10.5194/acp-12-2933-2012>, 2012.
- 1085 Holben, B. N., Eck, T. F., Slutsker, I., Tanré, D., Buis, J. P., Setzer, A., Vermote, E., Reagan, J. A., Kaufman, Y. J., Nakajima, T., Lavenu, F., Jankowiak, I., and Smirnov, A.: AERONET - A federated instrument network and data archive for aerosol characterization, *Remote Sensing of Environment*, 66, 1–16, [https://doi.org/10.1016/S0034-4257\(98\)00031-5](https://doi.org/10.1016/S0034-4257(98)00031-5), 1998.
- Hsu, N. C., Tsay, S. C., King, M. D., and Herman, J. R.: Aerosol properties over bright-reflecting source regions, *IEEE Transactions on Geoscience and Remote Sensing*, 42, 557–569, <https://doi.org/10.1109/TGRS.2004.824067>, 2004.
- 1090 Hsu, N. C., Jeong, M. J., Bettenhausen, C., Sayer, A. M., Hansell, R., Seftor, C. S., Huang, J., and Tsay, S. C.: Enhanced Deep Blue aerosol retrieval algorithm: The second generation, *Journal of Geophysical Research Atmospheres*, 118, 9296–9315, <https://doi.org/10.1002/jgrd.50712>, 2013.
- Huneeus, N., Schulz, M., Balkanski, Y., Griesfeller, J., Prospero, J., Kinne, S., Bauer, S., Boucher, O., Chin, M., Dentener, F., Diehl, T., Easter, R., Fillmore, D., Ghan, S., Ginoux, P., Grini, A., Horowitz, L., Koch, D., Krol, M. C., Landing, W., Liu, X., Mahowald, N., Miller, R., Morcrette, J. J., Myhre, G., Penner, J., Perlwitz, J., Stier, P., Takemura, T., and Zender, C. S.: Global dust model intercomparison in AeroCom phase I, *Atmospheric Chemistry and Physics*, 11, 7781–7816, <https://doi.org/10.5194/acp-11-7781-2011>, 2011.
- 1095 Hunt, B. R., Kostelich, E. J., and Szunyogh, I.: Efficient data assimilation for spatiotemporal chaos: A local ensemble transform Kalman filter, *Physica D: Nonlinear Phenomena*, 230, 112–126, <https://doi.org/10.1016/j.physd.2006.11.008>, 2007.
- Iacono, M. J., Mlawer, E. J., and Clough, S. A.: Validation of the RRTM Shortwave Radiation Model and Comparison to GCM Shortwave Models, *Eleventh ARM Science Team Meeting Proceedings*, 2, 1–6, 2001.
- 1100 Iacono, M. J., Delamere, J. S., Mlawer, E. J., Shephard, M. W., Clough, S. A., and Collins, W. D.: Radiative forcing by long-lived greenhouse gases: Calculations with the AER radiative transfer models, *Journal of Geophysical Research Atmospheres*, 113, 1–8, <https://doi.org/10.1029/2008JD009944>, 2008.
- Ito, A. and Shi, Z.: Delivery of anthropogenic bioavailable iron from mineral dust and combustion aerosols to the ocean, *Atmospheric Chemistry and Physics*, 16, 85–99, <https://doi.org/10.5194/acp-16-85-2016>, 2016.
- 1105 Ito, A. and Wagai, R.: Data Descriptor: Global distribution of clay-size minerals on land surface for biogeochemical and climatological studies, *Scientific Data*, 4, 1–11, <https://doi.org/10.1038/sdata.2017.1031>, 2017.
- Ito, A. and Xu, L.: Response of acid mobilization of iron-containing mineral dust to improvement of air quality projected in the future, *Atmospheric Chemistry and Physics*, 14, 3441–3459, <https://doi.org/10.5194/acp-14-3441-2014>, 2014.
- 1110 Ito, A., Lin, G., and Penner, J. E.: Radiative forcing by light-absorbing aerosols of pyrogenetic iron oxides, *Scientific Reports*, 8, 1–11, <https://doi.org/10.1038/s41598-018-25756-3>, 2018.
- Janjic, Z.: Nonsingular Implementation of the Mellor-Yamada Level 2.5 Scheme in the NCEP Meso model, *NCEP Office Note*, 437, 61, <http://www.emc.ncep.noaa.gov/officenotes/newernotes/on437.pdf>, 2002.
- Janjic, Z. and Gall, R.: Scientific Documentation of the NCEP Nonhydrostatic Multiscale Model on the B grid (NMMB). Part 1 Dynamics, *NCAR TECH. NOTE*, pp. 1–80, <https://doi.org/10.5065/D6WH2MZX>, 2012.
- 1115 Jickells, T. D.: Global Iron Connections Between Desert Dust, Ocean Biogeochemistry, and Climate, *Science*, 308, 67–71, <https://doi.org/10.1126/science.1105959>, 2005.
- Johnson, M. S. and Meskhidze, N.: Atmospheric dissolved iron deposition to the global oceans: Effects of oxalate-promoted Fe dissolution, photochemical redox cycling, and dust mineralogy, *Geoscientific Model Development*, 6, 1137–1155, [https://doi.org/10.5194/gmd-6-](https://doi.org/10.5194/gmd-6-1137-2013)
- 1120 1137-2013, 2013.

- Jorba, O., Dabdub, D., Blaszcak-Boxe, C., Pérez, C., Janjic, Z., Baldasano, J. M., Spada, M., Badia, A., and Gonçalves, M.: Potential significance of photoexcited NO<sub>2</sub> on global air quality with the NMMB/BSC chemical transport model, *Journal of Geophysical Research*, 117, D13 301, <https://doi.org/10.1029/2012JD017730>, 2012.
- Journet, E., Desboeufs, K. V., Caquineau, S., and Colin, J. L.: Mineralogy as a critical factor of dust iron solubility, *Geophysical Research Letters*, 35, 3–7, <https://doi.org/10.1029/2007GL031589>, 2008.
- Journet, E., Balkanski, Y., and Harrison, S. P.: A new data set of soil mineralogy for dust-cycle modeling, *Atmospheric Chemistry and Physics*, 14, 3801–3816, <https://doi.org/10.5194/acp-14-3801-2014>, 2014.
- Kanakidou, M., Myriokefalitakis, S., and Tsigaridis, K.: Aerosols in atmospheric chemistry and biogeochemical cycles of nutrients, *Environmental Research Letters*, 13, <https://doi.org/10.1088/1748-9326/aabdb>, 2018.
- Kandler, K., Benker, N., Bundke, U., Cuevas, E., Ebert, M., Knippertz, P., Rodríguez, S., Schütz, L., and Weinbruch, S.: Chemical composition and complex refractive index of Saharan Mineral Dust at Izaña, Tenerife (Spain) derived by electron microscopy, *Atmospheric Environment*, 41, 8058–8074, <https://doi.org/10.1016/j.atmosenv.2007.06.047>, 2007.
- Kandler, K., Schütz, L., Deutscher, C., Ebert, M., Hofmann, H., Jäckel, S., Jaenicke, R., Knippertz, P., Lieke, K., Massling, A., Petzold, A., Schladitz, A., Weinzierl, B., Wiedensohler, A., Zorn, S., and Weinbruch, S.: Size distribution, mass concentration, chemical and mineralogical composition and derived optical parameters of the boundary layer aerosol at Tinfou, Morocco, during SAMUM 2006, *Tellus, Series B: Chemical and Physical Meteorology*, 61, 32–50, <https://doi.org/10.1111/j.1600-0889.2008.00385.x>, 2009.
- Kandler, K., Schneiders, K., Heuser, J., Waza, A., Aryasree, S., Althausen, D., Hofer, J., Abdullaev, S. F., and Makhmudov, A. N.: Differences and Similarities of Central Asian, African, and Arctic Dust Composition from a Single Particle Perspective, *Atmosphere*, 11, 1–16, <https://doi.org/10.3390/atmos11030269>, 2020.
- Klose, M., Jorba, O., Gonçalves Ageitos, M., Escribano, J., Dawson, M. L., Obiso, V., Di Tomaso, E., Basart, S., Montané Pinto, G., MacChia, F., Ginoux, P., Guerschman, J., Prigent, C., Huang, Y., Kok, J. F., Miller, R. L., and Pérez García-Pando, C.: Mineral dust cycle in the Multiscale Online Nonhydrostatic Atmosphere Chemistry model (MONARCH) version 2.0, *Geoscientific Model Development*, 14, 6403–6444, <https://doi.org/10.5194/gmd-14-6403-2021>, 2021.
- Kok, J. F.: A scaling theory for the size distribution of emitted dust aerosols suggests climate models underestimate the size of the global dust cycle, *Proceedings of the National Academy of Sciences of the United States of America*, 108, 1016–1021, <https://doi.org/10.1073/pnas.1014798108>, 2011.
- Kok, J. F., Mahowald, N. M., Fratini, G., Gillies, J. A., Ishizuka, M., Leys, J. F., Mikami, M., Park, M. S., Park, S. U., Van Pelt, R. S., and Zobeck, T. M.: An improved dust emission model - Part 1: Model description and comparison against measurements, *Atmospheric Chemistry and Physics*, 14, 13 023–13 041, <https://doi.org/10.5194/acp-14-13023-2014>, 2014.
- Kok, J. F., Adebisi, A. A., Albani, S., Balkanski, Y., Checa-Garcia, R., Chin, M., Colarco, P. R., Hamilton, D. S., Huang, Y., Ito, A., Klose, M., Li, L., Mahowald, N. M., Miller, R. L., Obiso, V., Pérez García-Pando, C., Rocha-Lima, A., and Wan, J. S.: Contribution of the world’s main dust source regions to the global cycle of desert dust, *Atmospheric Chemistry and Physics*, 21, 8169–8193, <https://doi.org/10.5194/acp-21-8169-2021>, 2021.
- Krueger, B. J., Grassian, V. H., Cowin, J. P., and Laskin, A.: Heterogeneous chemistry of individual mineral dust particles from different dust source regions: The importance of particle mineralogy, *Atmospheric Environment*, 38, 6253–6261, <https://doi.org/10.1016/j.atmosenv.2004.07.010>, 2004.

- Lafon, S., Sokolik, I. N., Rajot, J. L., Caquinau, S., Gaudichet, A., Caquineau, S., and Gaudichet, A.: Characterization of iron oxides in mineral dust aerosols: Implications for light absorption, *Journal of Geophysical Research Atmospheres*, 111, 1–19, <https://doi.org/10.1029/2005JD007016>, 2006.
- 1160 Lawrence, C. R. and Neff, J. C.: The contemporary physical and chemical flux of aeolian dust: A synthesis of direct measurements of dust deposition, *Chemical Geology*, 267, 46–63, <https://doi.org/10.1016/j.chemgeo.2009.02.005>, 2009.
- Li, L., Mahowald, N., Miller, R., Pérez García-Pando, C., Klose, M., Hamilton, D., Gonçalves Ageitos, M., Ginoux, P., Balkanski, Y., Green, R., Kalashnikova, O., Kok, J., Obiso, V., Paynter, D., and Thompson, D.: Quantifying the range of the dust direct radiative effect due to source mineralogy uncertainty, *Atmospheric Chemistry and Physics*, 21, 3973–4005, <https://doi.org/10.5194/acp-21-3973-2021>, 2021.
- 1165 Longtin, D. R., Shettle, E. P., Hummel, J. R., and Pryce, J. D.: A wind dependent desert aerosol model: radiative properties, Technical report afgl-tr-88-0112, Air Force Geophysics Laboratory, Hanscom AFB, Massachussets, 1988.
- Luo, C., Mahowald, N., Bond, T., Chuang, P. Y., Artaxo, P., Siefert, R., Chen, Y., and Schauer, J.: Combustion iron distribution and deposition, *Global Biogeochemical Cycles*, 22, <https://doi.org/10.1029/2007GB002964>, 2008.
- Mahowald, N., Jickells, T. D., Baker, A. R., Artaxo, P., Benitez-Nelson, C. R., Bergametti, G., Bond, T. C., Chen, Y., Cohen, D. D., Herut, B., Kubilay, N., Losno, R., Luo, C., Maenhaut, W., McGee, K. A., Okin, G. S., Siefert, R. L., and Tsukuda, S.: Global distribution of atmospheric phosphorus sources, concentrations and deposition rates, and anthropogenic impacts, *Global Biogeochemical Cycles*, 22, 1–19, <https://doi.org/10.1029/2008GB003240>, 2008.
- 1170 Mahowald, N. M., Engelstaedter, S., Luo, C., Sealy, A., Artaxo, P., Benitez-Nelson, C., Bonnet, S., Chen, Y., Chuang, P. Y., Cohen, D. D., Dulac, F., Herut, B., Johansen, A. M., Kubilay, N., Losno, R., Maenhaut, W., Paytan, A., Prospero, J. M., Shank, L. M., and Siefert, R. L.: Atmospheric iron deposition: global distribution, variability, and human perturbations., *Annual review of marine science*, 1, 245–278, <https://doi.org/10.1146/annurev.marine.010908.163727>, 2009.
- Manubens-Gil, D., Vegas-Regidor, J., Prodhomme, C., Mula-Valls, O., and Doblas-Reyes, F. J.: Seamless Management of Ensemble Climate Prediction Experiments on HPC Platforms, in: 2016 International Conference on High Performance Computing and Simulation (HPCS), pp. 895–900, IEEE, Innsbruck, <https://doi.org/10.1109/HPCSim.2016.7568429>, 2016.
- 1180 Marticorena, B. and Bergametti, G.: Modeling the atmospheric dust cycle: 1. Design of a soil-derived dust emission scheme, *Journal of Geophysical Research*, 100, 16 415–16 430, <https://doi.org/10.1029/95jd00690>, 1995.
- Marticorena, B., Chatenet, B., Rajot, J. L., Traoré, S., Coulibaly, M., Diallo, A., Koné, I., Maman, A., Ndiaye, T., and Zakou, A.: Temporal variability of mineral dust concentrations over West Africa: Analyses of a pluriannual monitoring from the AMMA Sahelian Dust Transect, *Atmospheric Chemistry and Physics*, 10, 8899–8915, <https://doi.org/10.5194/acp-10-8899-2010>, 2010.
- 1185 Mellor, G. L. and Yamada, T.: Development of a turbulence closure model for geophysical fluid problems, <https://doi.org/10.1029/RG020i004p00851>, 1982.
- Menut, L., Siour, G., Bessagnet, B., Couvidat, F., Journet, E., Balkanski, Y., and Desboeufs, K.: Modelling the mineralogical composition and solubility of mineral dust in the Mediterranean area with CHIMERE 2017r4, *Geoscientific Model Development*, 13, 2051–2071, <https://doi.org/10.5194/gmd-13-2051-2020>, 2020.
- 1190 Miller, R. L., Knippertz, P., García-Pando, C. P., Perlwitz, J. P., and Tegen, I.: Mineral Dust, <https://doi.org/10.1007/978-94-017-8978-3>, 2014.
- Miyoshi, T. and Yamane, S.: Local ensemble transform Kalman filtering with an AGCM at a T159/L48 resolution, *Monthly Weather Review*, 135, 3841–3861, <https://doi.org/10.1175/2007MWR1873.1>, 2007.

- Moosmuller, H., Engelbrecht, J. P., Skiba, M., Frey, G., Chakrabarty, R. K., and Arnott, W. P.: Single scattering albedo  
1195 of fine mineral dust aerosols controlled by iron concentration, *Journal of Geophysical Research Atmospheres*, 117, 1–10,  
<https://doi.org/10.1029/2011JD016909>, 2012.
- Myriokefalitakis, S., Daskalakis, N., Mihalopoulos, N., Baker, A. R., Nenes, A., and Kanakidou, M.: Changes in dissolved iron deposition to  
the oceans driven by human activity: a 3-D global modelling study, *Biogeosciences*, 12, 3973–3992, [https://doi.org/10.5194/bg-12-3973-](https://doi.org/10.5194/bg-12-3973-2015)  
2015, 2015.
- 1200 Myriokefalitakis, S., Ito, A., Kanakidou, M., Nenes, A., Krol, M. C., Mahowald, N. M., Scanza, R. A., Hamilton, D. S., Johnson, M. S.,  
Meskhidze, N., Kok, J. F., Guieu, C., Baker, A. R., Jickells, T. D., Sarin, M. M., Bikkina, S., Shelley, R., Bowie, A., Perron, M. M.,  
and Duce, R. A.: Reviews and syntheses: The GESAMP atmospheric iron deposition model intercomparison study, *Biogeosciences*, 15,  
6659–6684, <https://doi.org/10.5194/bg-15-6659-2018>, 2018.
- Myriokefalitakis, S., Bergas-Massó, E., Gonçalves Ageitos, M., and García-Pando, C. P.: Multiphase processes in the EC-Earth model  
1205 and their relevance to the atmospheric oxalate , sulfate , and iron cycles, *Geoscientific Model Development*, pp. 3079–3120,  
<https://doi.org/10.5194/gmd-15-3079-2022>, 2022.
- Navarro-Barboza, H., Pandolfi, M., and Jorba, O.: Constraining the chemical composition of particulate matter in an atmospheric chemistry  
model, in: 8th BSC Doctoral Symposium, edited by BSC, pp. 50–51, Barcelona, <http://hdl.handle.net/2117/346338>, 2021.
- Nickovic, S., Vukovic, A., Vujadinovic, M., Djurdjevic, V., and Pejanovic, G.: Technical Note: High-resolution mineralogical database of  
1210 dust-productive soils for atmospheric dust modeling, *Atmospheric Chemistry and Physics*, 12, 845–855, [https://doi.org/10.5194/acp-12-](https://doi.org/10.5194/acp-12-845-2012)  
845-2012, 2012.
- Obiso, V., Gonçalves Ageitos, M., Pérez García-Pando, C., Schuster, G. L., Bauer, S. E., Di Biagio, C., Formenti, P., Perlwitz, J. P., Tsigaridis,  
K., and Miller, R. L.: Observationally constrained regional variations of shortwave absorption by iron oxides emphasize the cooling effect  
of dust, *Atmospheric Chemistry and Physics*, submitted preprint at EGUSPHERE-2023-1166, 2023.
- 1215 Obiso, V., Gonçalves Ageitos, M., Miller, R. L., Pérez García-Pando, C., Schuster, G. L., Bauer, S. E., Di Biagio, C., Formenti, P., Jorba, O.,  
Perlwitz, J. P., and Tsigaridis, K.: Regional variations in dust shortwave absorption explained predominantly by mineralogical composition,  
tbd, in prep.
- Panta, A., Kandler, K., Alastuey, A., González-flórez, C., González-romero, A., Klose, M., Querol, X., Reche, C., Yús-díez, J., and  
García-pando, C. P.: Insights into the single particle composition, size, mixing state and aspect ratio of freshly emitted mineral  
1220 dust from field measurements in the Moroccan Sahara using electron microscopy, *Atmospheric Chemistry and Physics Discussions*,  
<https://acp.copernicus.org/preprints/acp-2022-742/>, 2022.
- Pérez, C., Haustein, K., Janjic, Z., Jorba, O., Huneeus, N., Baldasano, J. M., Black, T., Basart, S., Nickovic, S., Miller, R. L., Perl-  
witz, J. P., Schulz, M., and Thomson, M.: Atmospheric dust modeling from meso to global scales with the online NMMB/BSC-  
Dust model; Part 1: Model description, annual simulations and evaluation, *Atmospheric Chemistry and Physics*, 11, 13 001–13 027,  
1225 <https://doi.org/10.5194/acp-11-13001-2011>, 2011.
- Pérez García-Pando, C., Miller, R. L., Perlwitz, J. P., Rodríguez, S., and Prospero, J. M.: Predicting the mineral composition of dust  
aerosols: Insights from elemental composition measured at the Izaña Observatory, *Geophysical Research Letters*, 43, 10,520–10,529,  
<https://doi.org/10.1002/2016GL069873>, 2016.
- Perlwitz, J. P., Pérez García-Pando, C., and Miller, R. L.: Predicting the mineral composition of dust aerosols - Part 1: Representing key  
1230 processes, *Atmospheric Chemistry and Physics*, 15, 11 593–11 627, <https://doi.org/10.5194/acp-15-11593-2015>, 2015a.

- Perlwitz, J. P., Pérez García-Pando, C., and Miller, R. L.: Predicting the mineral composition of dust aerosols - Part 2: Model evaluation and identification of key processes with observations, *Atmospheric Chemistry and Physics*, 15, 11 629–11 652, <https://doi.org/10.5194/acp-15-11629-2015>, 2015b.
- Prospero, J. M.: Mineral-Aerosol Transport to the North Atlantic and North Pacific: The Impact of African and Asian Sources, pp. 59–86, Springer Netherlands, Dordrecht, [https://doi.org/10.1007/978-94-009-0503-0\\_4](https://doi.org/10.1007/978-94-009-0503-0_4), 1990.
- Prospero, J. M.: The Atmospheric Transport of Particles to the Ocean, Wiley, New York, 1996.
- Prospero, J. M.: Long-term measurements of the transport of African mineral dust to the southeastern United States: Implications for regional air quality, *Journal of Geophysical Research Atmospheres*, 104, 15 917–15 927, <https://doi.org/10.1029/1999JD900072>, 1999.
- Querol, X., Alastuey, A., Lopez-Soler, A., Mantilla, E., and Plana, F.: Mineral composition of atmospheric particulates around a large coal-fired power station, *Atmospheric Environment*, 30, 3557–3572, [https://doi.org/10.1016/1352-2310\(96\)00108-2](https://doi.org/10.1016/1352-2310(96)00108-2), 1996.
- Rathod, S. D., Hamilton, D. S., Mahowald, N. M., Klimont, Z., Corbett, J. J., and Bond, T. C.: A Mineralogy-Based Anthropogenic Combustion-Iron Emission Inventory, *Journal of Geophysical Research: Atmospheres*, 125, 1–35, <https://doi.org/10.1029/2019JD032114>, 2020.
- Raupach, M. R., Gille, D. A., and Leys, J. F.: The effect of roughness elements on wind erosion threshold, *J. Geophys. Res.*, 98, 3023–3029, <https://doi.org/10.1029/92JD01922>, 1993.
- Scanza, R. A., Mahowald, N., Ghan, S., Zender, C. S., Kok, J. F., Liu, X., Zhang, Y., and Albani, S.: Modeling dust as component minerals in the Community Atmosphere Model: Development of framework and impact on radiative forcing, *Atmospheric Chemistry and Physics*, 15, 537–561, <https://doi.org/10.5194/acp-15-537-2015>, 2015.
- Scanza, R. A., Hamilton, D. S., Perez Garcia-Pando, C., Buck, C., Baker, A., and Mahowald, N. M.: Atmospheric processing of iron in mineral and combustion aerosols: Development of an intermediate-complexity mechanism suitable for Earth system models, *Atmospheric Chemistry and Physics*, 18, 14 175–14 196, <https://doi.org/10.5194/acp-18-14175-2018>, 2018.
- Scheuven, D., Schütz, L., Kandler, K., Ebert, M., and Weinbruch, S.: Bulk composition of northern African dust and its source sediments-A compilation, *Earth-Science Reviews*, 116, 170–194, <https://doi.org/10.1016/j.earscirev.2012.08.005>, 2013.
- Schuster, G. L., Dubovik, O., and Arola, A.: Remote sensing of soot carbon - Part 1: distinguishing different absorbing aerosol species, *Atmospheric Chemistry and Physics*, 16, 1565–1585, <https://doi.org/10.5194/acp-16-1565-2016>, 2016.
- Schutgens, N. A., Miyoshi, T., Takemura, T., and Nakajima, T.: Applying an ensemble Kalman filter to the assimilation of AERONET observations in a global aerosol transport model, *Atmospheric Chemistry and Physics*, 10, 2561–2576, <https://doi.org/10.5194/acp-10-2561-2010>, 2010.
- Shao, Y.: A model for mineral dust emission, *Journal of Geophysical Research*, 106, 20,239–20,254, <https://doi.org/10.1029/2001JD900171>, 2001.
- Shao, Y.: Simplification of a dust emission scheme and comparison with data, *Journal of Geophysical Research D: Atmospheres*, 109, 10 202, <https://doi.org/10.1029/2003JD004372>, 2004.
- Shao, Y., Ishizuka, M., Mikami, M., and Leys, J. F.: Parameterization of size-resolved dust emission and validation with measurements, *Journal of Geophysical Research: Atmospheres*, 116, 8203, <https://doi.org/10.1029/2010JD014527>, 2011.
- Shi, Z., Krom, M. D., Bonneville, S., Baker, A. R., Bristow, C., Drake, N., Mann, G., Carslaw, K., McQuaid, J. B., Jickells, T., and Benning, L. G.: Influence of chemical weathering and aging of iron oxides on the potential iron solubility of Saharan dust during simulated atmospheric processing, *Global Biogeochemical Cycles*, 25, <https://doi.org/10.1029/2010GB003837>, 2011.

- Shi, Z., Krom, M. D., Jickells, T. D., Bonneville, S., Carslaw, K. S., Mihalopoulos, N., Baker, A. R., and Benning, L. G.: Impacts on iron solubility in the mineral dust by processes in the source region and the atmosphere: A review, *Aeolian Research*, 5, 21–42, <https://doi.org/10.1016/j.aeolia.2012.03.001>, 2012.
- Sinyuk, A., Torres, O., and Dubovik, O.: Combined use of satellite and surface observations to infer the imaginary part of refractive index of Saharan dust, *Geophysical Research Letters*, 30, 1081, <https://doi.org/10.1029/2002GL016189>, 2003.
- Sinyuk, A., Holben, B. N., Eck, T. F., Giles, D. M., Slutsker, I., Korkin, S., Schafer, J. S., Smirnov, A., Sorokin, M., and Lyapustin, A.: The AERONET Version 3 aerosol retrieval algorithm, associated uncertainties and comparisons to Version 2, *Atmospheric Measurement Techniques*, 13, 3375–3411, <https://doi.org/10.5194/amt-13-3375-2020>, 2020.
- Slinn, W.: chap. Precipitation scavenging, in *Atmospheric Science and Power Production*, pp. 466 – 532, Tech. Inf. Cent., Off. of Sci. and Techn. Inf., Dep. of Energy, Washington DC, USA, 1984.
- Sokolik, I. N. and Toon, O. B.: Direct radiative forcing by anthropogenic airborne mineral aerosols, *Nature*, 381, 681–683, <https://doi.org/10.1038/381681a0>, 1996.
- Sokolik, I. N. and Toon, O. B.: Incorporation of mineralogical composition into models of the radiative properties of mineral aerosol from UV to IR wavelengths, *Journal of Geophysical Research: Atmospheres*, 104, 9423–9444, <https://doi.org/10.1029/1998JD200048>, 1999.
- Sokolik, I. N., Toon, O. B., and Bergstrom, R. W.: Modeling the radiative characteristics of airborne mineral aerosols at infrared wavelengths, *Journal of Geophysical Research Atmospheres*, 103, 8813–8826, <https://doi.org/10.1029/98JD00049>, 1998.
- Soussé Villa, R., Casellas, J., and Pérez García-Pando, C.: Modeling nitric acid uptake by mineral dust, in: 8th BSC Doctoral Symposium, edited by BSC, Barcelona, <https://doi.org/10.17077/etd.2xewzpnz>, 2021.
- Spada, M.: Development and evaluation of an atmospheric aerosol module implemented within the NMMB/BSC-CTM, Ph.D. thesis, Universitat Politècnica de Catalunya, <http://hdl.handle.net/2117/95991>, 2015.
- Spada, M., Jorba, O., Pérez García-Pando, C., Janjic, Z., and Baldasano, J. M.: Modeling and evaluation of the global sea-salt aerosol distribution: Sensitivity to emission schemes and resolution effects at coastal/orographic sites, *Atmospheric Chemistry and Physics*, 13, 11 735–11 755, <https://doi.org/10.5194/acp-13-11735-2013>, 2013.
- Uruchi, W., Castrillo, M., and Beltrán, D.: Autosubmit GUI: A Javascript-based Graphical User Interface to Monitor Experiments Workflow Execution, *Journal of Open Source Software*, 6, 3049, <https://doi.org/10.21105/joss.03049>, 2021.
- Usher, C. R., Al-Hosney, H., Carlos-Cuellar, S., and Grassian, V. H.: A laboratory study of the heterogeneous uptake and oxidation of sulfur dioxide on mineral dust particles, *Journal of Geophysical Research: Atmospheres*, 107, 1–9, <https://doi.org/10.1029/2002JD002051>, 2002.
- Vergara-Temprado, J., Murray, B. J., Wilson, T. W., O’sullivan, D., Browse, J., Pringle, K. J., Ardon-Dryer, K., Bertram, A. K., Burrows, S. M., Ceburnis, D., Demott, P. J., Mason, R. H., O’dowd, C. D., Rinaldi, M., and Carslaw, K. S.: Contribution of feldspar and marine organic aerosols to global ice nucleating particle concentrations, *Atmos. Chem. Phys.*, 17, 3637–3658, <https://doi.org/10.5194/acp-17-3637-2017>, 2017.
- Wagner, R., Ajtai, T., Kandler, K., Lieke, K., Linke, C., Müller, T., Schnaiter, M., and Vragel, M.: Complex refractive indices of Saharan dust samples at visible and near UV wavelengths: a laboratory study, *Atmospheric Chemistry and Physics*, 12, 2491–2512, <https://doi.org/10.5194/acp-12-2491-2012>, 2012.
- Wang, R., Balkanski, Y., Boucher, O., Bopp, L., Chappell, A., Ciais, P., Hauglustaine, D., Peñuelas, J., and Tao, S.: Sources, transport and deposition of iron in the global atmosphere, *Atmospheric Chemistry and Physics*, 15, 6247–6270, <https://doi.org/10.5194/acp-15-6247-2015>, 2015.

- 1305 Wang, Z., Pan, X., Uno, I., Li, J., Wang, Z., Chen, X., Fu, P., Yang, T., Kobayashi, H., Shimizu, A., Sugimoto, N., and Yamamoto, S.: Significant impacts of heterogeneous reactions on the chemical composition and mixing state of dust particles: A case study during dust events over northern China, *Atmospheric Environment*, 159, 83–91, <https://doi.org/10.1016/j.atmosenv.2017.03.044>, 2017.
- Weinbruch, S., Zou, L., Ebert, M., Benker, N., Drotikova, T., and Kallenborn, R.: Emission of nanoparticles from coal and diesel fired power plants on Svalbard: An electron microscopy study, *Atmospheric Environment*, 282, 119 138, <https://doi.org/10.1016/j.atmosenv.2022.119138>, 2022.
- 1310 Yu, H., Chin, M., Yuan, T., Bian, H., Remer, L. A., Prospero, J. M., Omar, A., Winker, D., Yang, Y., Zhang, Y., Zhang, Z., and Zhao, C.: The fertilizing role of African dust in the Amazon rainforest: A first multiyear assessment based on data from Cloud-Aerosol Lidar and Infrared Pathfinder Satellite Observations, *Geophysical Research Letters*, 42, 1984–1991, <https://doi.org/10.1002/2015GL063040>, 2015.
- Zakoura, M., Kakavas, S., Nenes, A., and Pandis, S.: Size-resolved aerosol pH over Europe during summer, *Atmospheric Chemistry and Physics*, pp. 1–24, <https://doi.org/10.5194/acp-2019-1146>, 2020.
- 1315 Zimmermann, F., Weinbruch, S., Schütz, L., Hofmann, H., Ebert, M., Kandler, K., and Wörzinger, A.: Ice nucleation properties of the most abundant mineral dust phases, *Journal of Geophysical Research*, 113, D23 204, <https://doi.org/10.1029/2008JD010655>, 2008.